Single Camera 3D Measurement of a Shock Wave-Turbulent Boundary Layer Interaction

by

Johnathan Bolton

A thesis submitted to the Graduate Faculty of
Auburn University
in partial fulfillment of the
requirements for the Degree of
Master of Science

Auburn, Alabama
May 6, 2017

Keywords: Plenoptic, Microlens, SBLI

Approved by

Brian Thurow, Chair, W. Allen and Martha Reed Associate Professor of Aerospace Engineering
David Scarborough, Assistant Professor of Aerospace Engineering
Anwar Ahmed, Professor of Aerospace Engineering

Abstract

This paper explores the 3D structure of an unswept fin generated shock wave-turbulent boundary layer interaction (SBLI). A Mach 2 flow encounters an unswept fin at an angle of attack of 15° which causes an inviscid, oblique shock wave with a wave angle of approximately 45°. The oblique shock wave introduced by the fin interacts with the turbulent boundary layer along the bottom surface. This interaction causes flow separation, and forms a λ-shaped shock structure. This structure has been studied extensively in quasi-2D representations, but the fully 3D structure has not been studied previously. A plenoptic camera is a unique diagnostic tool that captures 3D information using a single camera. This novel imaging system can be combined with particle image velocimetry to obtain 3D velocity data about a flow field. This work is the first application of a plenoptic camera for volumetric studies of SBLI, and it has proven the unique capabilities of the plenoptic camera to obtain 3D velocity information in areas of limited optical access and in supersonic flows. Comparison with stereo PIV data and inviscid shock theory show a good agreement.

Acknowledgments

I must begin by acknowledging the support of my friends and family. I would first like to thank my wife Lauren for her support throughout my time in Auburn. She has been such an excellent supporter and helper in all aspects of my life, and she has been particularly motivating as I have endeavored to publish this work. I would also like to thank my mother for listening as I described all of my work despite her lack of interest in this field. In addition, she has been a driving force throughout my work here as she has continually questioned the work that I have been doing and how much success I have been having. The rest of my family has been incredibly supportive and loving throughout this process, and they have continued to show confidence in me even when I didn't have much myself.

I also would like to acknowledge the support of all members of my laboratory. Kyle Johnson and Tim Fahringer have been extremely helpful with my data processing, and they have helped me to continually improve my programming and data visualization. Jenna Klemkowsky was a huge part of the success of this experiment. She was there during the experiment to help me set up all of the equipment and begin to analyze the data. Elise Hall was especially helpful with regard to my writing. I often went to her with questions for the flow of my papers and how to phrase my statements. Dr. Chris Clifford was a major point of advice regarding every part of my experiment and data processing, and his criticism has helped me to become a better engineer. Lastly, my advisor, Dr. Brian Thurow, has been supportive not only with regards to my work but with regards to the balance between my work and personal life. He has taught me many things about how to be a better engineer and colleague to everyone I work with.

Table of Contents

Abstract ii

Acknowledgments iii

List of Figures vi

1 Introduction 1

2 Background 7

2.1 SBLI Classifications and Structure 7

2.2 Cylindrically and Conically Symmetric SBLI 8

2.2.1 Unswept and Swept Fins 8

2.2.2 Compression Corners 11

2.2.3 Semi-Cones 13

2.3 Experimental and Computational Results of Conically Symmetric SBLI . . . 14

2.3.1 Hainsworth, et al. 14

2.3.2 Fang, et al. 17

2.3.3 Alvi and Settles 1990 23

2.3.4 Alvi and Settles 1992 28

2.3.5 Arora, et. al 30

3 Experimental Setup 34

3.1 Wind Tunnel Facility 34

3.2 Stereo PIV 35

3.3 Plenoptic PIV 36

4 Results 41

4.1 Comparison with Inviscid Shock Relations 43

4.1.1 Streamwise Velocity Field 43

4.1.2 Spanwise Velocity Field 44
4.2 Comparison with Stereo PIV Measurements 46
4.3 Separation Bubble 49
4.4 3D Relieving Effect 50
4.5 RMS Velocity Fluctuations 53
5 Conclusions and Future Work 56
Bibliography 58

List of Figures

1.1 Diagram of an Unswept Fin-Generated SBLI Flow Field [1] 3

1.2 Structure of Unswept Fin-Generated SBLI [2] 4

2.1 Surface Pressure Distribution and Interaction Map of Unswept Fin-Generated SBLI [3] 9

2.2 Primary and Secondary Separation Conditions [3] 10

2.3 Unswept Fin SBLI Structure [3] 11

2.4 Propagation Angles of SBLI Major Features [3] 12

2.5 Interaction Symmetry Conditions [3] 13

2.6 Surface Pressure Distribution for a Swept Compression Corner [3] 14

2.7 Plots of Swept Wedge Experimental Setup [4] 15

2.8 Unswept and Swept Wedge SBLI Structure [4] 16

2.9 Vertical Velocity Contour Plots From Unswept and Swept Wedge SBLI Experiments [4] 17

2.10 Plots of Unswept Fin Computational Setup [5] 18

2.11 Surface Pressure and Skin Friction Distribution From Computational Study of Unswept Fin-Generated SBLI [5] 19

2.12 Instantaneous Numerical Schlieren From Computational Study of Unswept Fin-Generated SBLI [5] 20

2.13 Mean Numerical Schlieren From Computational Study of Unswept Fin-Generated SBLI [5] 21

2.14 Streamlines of the Shock-Normal Velocity in an Unswept Fin-Generated SBLI [5] 21

2.15 Contours of Pressures and Normal Mach Number in an Unswept Fin-Generated SBLI [5] 22

2.16 Conical Shadowgraphy Images of an Unswept Fin-Generated SBLI at Varying Normal Mach Numbers [2] 24

2.17 Composite Shadowgraph and Surface Pressure Distribution of an Unswept Fin-Generated SBLI [2] 26

2.18 Plots of Separation and Rear Shock Angles Vs. Normal Mach Number for an Unswept Fin-Generated SBLI [2] 27

2.19 Sketch of Unswept Fin-Generated Interaction Features [2] 27

2.20 Contours of Pressures and Normal Mach Number in an Unswept Fin-Generated SBLI [6] 29

2.21 Planar and Stereo PIV Experimental Setup [1] 30

2.22 Surface Oil Flow Visualization of Unswept Fin-Generated SBLI [1] 31

2.23 Top View of Experimental Arrangement for Planar PIV [1] 31

2.24 Shock-Normal Velocity Contours [1] 32

2.25 Shock-Normal Velocity Contour and profile at various x' distances [1] 33

3.1 Stereo PIV Experimental Arrangement [7] 35

3.2 Experimental Setup Photo and Diagram 37

3.3 Slices of Volume with Differing Reconstruction Methods 39

4.1 Isosurfaces of Velocity Magnitude 42

4.2 Slices of Component Velocities at Z=12.5 mm 45

4.3 Slices of In-Plane and Out-of-Plane Velocity from Stereo PIV and Plenoptic PIV 48

4.4 Isosurfaces of Velocity Magnitude And Slice of Wall-Normal Velocity at 14.4 mm 50

4.5 Slices of Wall-Normal Velocity and Isosurfaces of Velocity Magnitude 51

4.6 Isosurface and Slices of RMS Streamwise Velocity Fluctuations 55

Chapter 1

Introduction

The interaction of a shock wave and a turbulent boundary layer is a ubiquitous occurrence in the flight of supersonic aircraft. It is commonly assumed that the first reference to this possible interaction was written by Antonio Ferri in 1939 [8, 9]. The discovery of this complex interaction was a simple first step in the motivation of more than 60 years of research. The interaction of a supersonic artifact such as a shock wave and a subsonic flow such as a boundary layer is a unique field of study. Wing-fuselage junctions, inlets, and diffusers are excellent examples of SBLI-forming structures. These areas often experience detrimental effects such as flow separation, enhanced heat transfer, and pressure losses. Early in the development of supersonic aircraft, the detrimental effects of supersonic flight became apparent. One example is the hypersonic X-15. During testing of a high-speed research engine, which was mounted below the fuselage, an impinging shock burned through the attachment causing the engine to separate from the plane. Had the engine remained attached, it is very likely that a hole would have burned in the fuselage, which would cause the X-15 to fall apart in flight. [10, 11] Throughout continued development of supersonic aircraft, the problems associated with the interaction of shock waves and boundary layers became readily apparent, and these problems spurred more than 60 years of research.

While some SBLI are quasi-2D structures, the large majority of SBLI encountered on supersonic vehicles are inherently 3D. The largest portion of prior research into SBLI has been concentrated on the quasi-2D interactions. While the structure of quasi-2D interactions is a significant portion of the necessary knowledge regarding SBLI, the fact that a large number of the commonly encountered SBLI are inherently 3D should encourage studies of these truly 3D interactions. Current studies are indeed beginning to recognize the importance

of the three-dimensionality of SBLI, and modern developments in 3D imaging technologies have enabled these studies. The entirety of past research into the quasi-2D interactions has provided the base of knowledge for progress in 3D studies. Prior literature from Settles and Dolling [3] detailed the types of swept interactions and classified them into semi-infinite and non-semi-infinite groups. The semi-infinite interactions were further classified into dimensional and dimensionless interactions. When an increase in the shock generator dimensions would not result in changes in the interaction properties, the interaction is termed semi-infinite. In contrast, a non-semi-infinite interaction is one in which a change in the shock generator dimensions would result in changes in the interaction properties, such as small protuberances. If the shock generator does not impose a length scale on the interaction, it is termed dimensionless. Some form of symmetry is exhibited in a large number of dimensionless interactions. For swept interactions, conical symmetry is the most common form, but cylindrical symmetry may be exhibited particularly at low angles of attack.

The study detailed here is a volumetric particle image velocimetry (PIV) study of an unswept fin generated SBLI. An unswept fin is placed in a Mach 2 flow which generates a planar oblique shock wave. The interaction of interest here is the interaction propagating from the base of the fin. The interaction is swept downstream along the oblique shock angle. The fin leading edge is perfectly orthogonal to the test section surface. The fin and interaction features are shown graphically in Figure 1.1. This figure comes from a previous study in the same facility and flow geometry using a planar PIV technique. [1] The free stream flow is at Mach 2, and the fin's angle of attack is 15°. This combination results in a planar oblique shock wave at a wave angle of approximately 45° with respect to the free stream. The interaction between the shock wave and the boundary layer on the test section floor results in a λ-shaped structure, such as that shown in Figure 1.2. There is an adverse pressure gradient due to the presence of the shock wave. This results in boundary layer separation, marked as vortex in Figure 1.2, as the boundary layer begins to turn upwards against this gradient. The separation of the boundary layer flow occurs below the inviscid

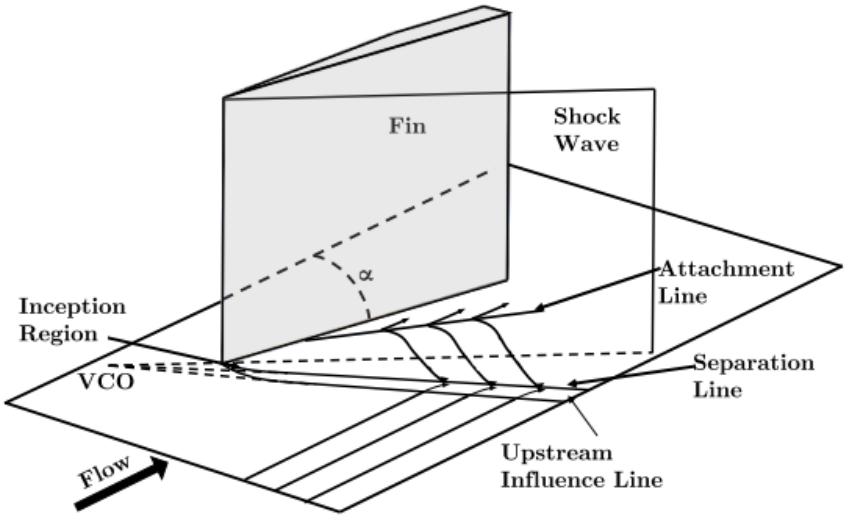

Figure 1.1: Diagram of an Unswept Fin-Generated SBLI Flow Field [1]

shock and requires an upstream shock in order to turn some of the flow above the separation bubble. This upstream shock is termed the separation shock, and it is the upstream portion of the λ structure. The flow turning upward around the separation bubble encounters the horizontal flow behind the inviscid shock wave, and this interaction necessitates the formation of another shock wave in order to align the two flows. This is the rear shock, and it is the bottom leg of the λ structure. The flow behind the rear shock and the inviscid shock interact to form a slip line. While this interaction has been studied extensively enough to provide the image in Figure 1.2, the full three-dimensionality of the interaction has not seen considerable study.

Quasi-conical symmetry has been seen in previous literature with similar structures. [2, 12, 13] The presence of quasi-conical symmetry shows the inherently 3D nature of this interaction. This symmetry is not limited to unswept fin generated interactions. It is seen in other shock generators such as swept compression corners, swept wedges, and semi-cones. The symmetry of many SBLI is often exploited by researchers through novel experimental techniques which provide quasi-2D views of the interaction while developing knowledge of the three-dimensionality. One example of this exploitation was the study of Hainsworth, et al. [4]. The authors used planar PIV at varying spanwise planes in the test section in

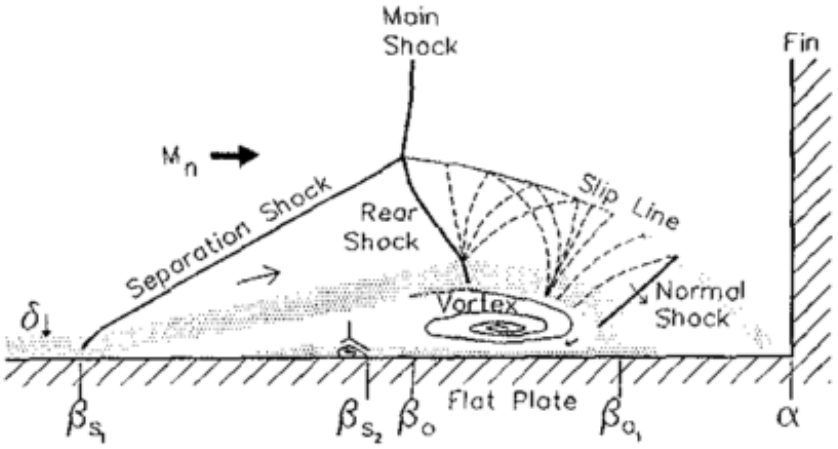

Figure 1.2: Structure of Unswept Fin-Generated SBLI [2]

order to determine the change in the interaction structure at different planes. While not a 3D technique, the use of planar PIV exploits the symmetry by shifting the planes in the streamwise direction for given shifts in spanwise direction. Planar PIV was also used by Arora, et al. [1] albeit in a different perspective and different geometry. In this study, the planes were aligned normal to the shock wave, and multiple planes of data were captured in order to view the 3D effects. Yet another exploration of conically symmetric SBLI, and perhaps the truest exploitation of the symmetry, comes from the conical shadowgraphy study of Alvi and Settles. [2] Instead of traditional shadowgraphy (wherein a collimated beam of light is passed through the test section), conical shadowgraphy focuses the collimated beam to a single point in the volume thus spreading the light in a cone from this single point. In this experiment, the cone was focused to the virtual conical origin which is slightly upstream of the fin apex. The virtual conical origin is the imaginary point where the lines of symmetry of the inviscid shock, separation shock, and reattachment line intersect. Because the cone was focused to this point it aligned directly with the cone of symmetry of the interaction, and this alignment provided a quasi-2D representation of the interaction. Figure 1.2 as discussed above is taken from the conical shadowgraphy results. This figure shows all of the major features, to include the separation shock, rear shock, and slip region. This study

displayed the presence of a normal shock below the slip line, which is an element of the interaction unique to high Mach number flows. The normal shock below the slip line forms as a consequence of the impinging jet flow on the test section surface. This study also viewed the secondary separation (β_{S_2}), which was previously defined as another element of high Mach number interactions. Both of these elements of high Mach number flows are not present in the experiment detailed here, but they are worthy elements of description in terms of the overall SBLI structure.

The necessity of fully 3D studies of SBLI restricts the possibilities in terms of experimental techniques which may be applied. All of the previously mentioned experimental studies utilized some technique which results in a quasi-2D representation or which does not capture the full 3D velocity field. Stereo PIV, 2D scanning techniques and line of sight measurements may provide some information, but the complete picture of the 3D velocity field can only be elucidated through the application of a fundamentally 3D measurement technique. The largest restriction on the application of 3D measurement techniques has been the requirement of large angular separation between multiple cameras. Many supersonic wind tunnels and facilities have very small areas of optical access which does not allow multiple cameras to maintain the necessary angles and image the same volume. The plenoptic camera is a unique tool capable of meeting the need for 3D information in an area of small optical access. A single plenoptic camera is capable of capturing the full light field in a scene. [14, 15] Plenoptic cameras have benefits even in flows that have the necessary areas of optical access for other techniques. There is a much simpler setup and calibration during the experimental process with the use of plenoptic cameras. Previous studies [16] have shown the capabilities of plenoptic cameras in liquid flows, and the present work seeks to expand upon the previous literature by applying a plenoptic camera in a supersonic flow.

Plenoptic PIV combines a plenoptic camera with particle image velocimetry to obtain a 3D velocity field. A plenoptic camera captures the position and angle of the light rays entering the camera, and this information can be used to computationally reconstruct a

particle volume as discussed in Fahringer, et al. [17] Generally the most well-known feature of plenoptic cameras is computational refocusing. A single image taken with a plenoptic camera can be computationally refocused to different planes in the scene. The ability of a single plenoptic camera to capture 3D information is extremely useful with regards to flow facilities with limited optical access. Where some techniques such as tomographic PIV may be limited due to insufficient optical access, a single plenoptic camera may be able to capture 3D information. The limited angles of light captured by a single camera lens do affect plenoptic PIV results in that a reconstructed particle is generally elongated along the camera axis. This produces some error in the cross correlation as the particles are not reconstructed as perfect spheres but as prolate spheroids. Previous studies [17, 18] in the AFDL have shown this elongation to result in minimal error, and it was previously shown that in this particular work, the results are not appreciably affected. [19]

Plenoptic PIV shares many similarities with traditional planar PIV. The major difference between planar and plenoptic PIV is the addition of a second cylindrical lens 90° opposed to the first in order to spread the laser in two directions. Otherwise, the camera and laser arrangement remains the same. The plenoptic camera's unique abilities lead to the visualization of a fully 3D velocity field with a similar experimental setup to planar PIV.

Chapter 2

Background

2.1 SBLI Classifications and Structure

Classifications for swept SBLI have been previously described by Settles and Dolling. [3] The major classifications are semi-infinite and non-semi-infinite, and within the semi-infinite classification a subdivision exists between dimensional and dimensionless interactions. Semi-infinite interactions refer to those SBLI in which the shock generator is large enough that increases in the generator dimensions would not result in changes to the interaction. One example of these is an unswept fin-generated SBLI. In the case of a sufficiently large fin, any increase in the fin's length or height would not change the dimensions of the SBLI. In contrast, non-semi-infinite SBLI are those interactions where a change in the shock generator geometry would result in changes to the interaction. An example of non-semi-infinite interactions is small protuberances. As the height of a small protuberance is increased, the SBLI takes a very different structure and dimension.

Dimensional interactions are those SBLI in which the shock generator imposes a length scale on the interaction. In contrast to dimensionless interactions such as sharp fins, these generators cause a significant scaling of the interaction. For a sharp unswept fin, the major lengths such as the fin length do not matter to the interaction. In this case, the flow experiences a compression, and it does not have any consideration for the length of the fin which causes that compression. Although there is an inception zone with a certain curvature, this curvature does not correspond to any dimension of the fin itself. Any change in the dimensions of the fin (length, height, etc.) results in no change in the curvature of the inception zone. In contrast, a blunt fin results in a particular curvature of the interaction which is inherently tied to the diameter of the fin's leading edge. An increase in this diameter

would result in a change in the curvature of the interaction, and this length scaling is what makes the interaction dimensional.

2.2 Cylindrically and Conically Symmetric SBLI

2.2.1 Unswept and Swept Fins

A sharp unswept fin at an angle of attack α generates a planar oblique shock wave at a wave angle β_0. At a small angle of attack, this interaction does not cause boundary layer separation, but separation does occur at relatively moderate angles. The shock foot formed is a λ-type structure with an upstream shock (or separation shock) which forms at an angle β_S with respect to an imaginary point called the virtual conical origin. The virtual conical origin is the intersection of an extension of the lines of the upstream influence, shock, and reattachment. The reattachment occurs along a line at an angle β_A. These shock generators generally result in conical symmetry at some distance away from the fin edge, but an inception zone exists near the edge where little to no symmetry occurs. The inception zone can be seen in the curvature at the beginning of the separation shock (interaction start) line in Figure 2.1. The inception zone is the reason that the virtual conical origin is upstream of the fin apex. The curvature of this forward line causes the separation shock's symmetry line downstream to be forward of the fin apex.

Figure 2.1 shows the flow geometry and surface pressure distribution for a sharp unswept fin SBLI. The surface pressure distribution from left to right is as viewed from the fin toward the side wall. The pressure increases across the separation shock and decreases in the separation vortex. It then increases behind the inviscid and rear shocks before slightly decreasing just in front of the fin. All of these effects are intuitive from basic knowledge regarding compressible flows. In the case of shock waves, it is known that there is a pressure increase, and this feature is exhibited in the separation shock, inviscid shock, and rear shock. In the case of the separation bubble the vortex creates the change in pressure.

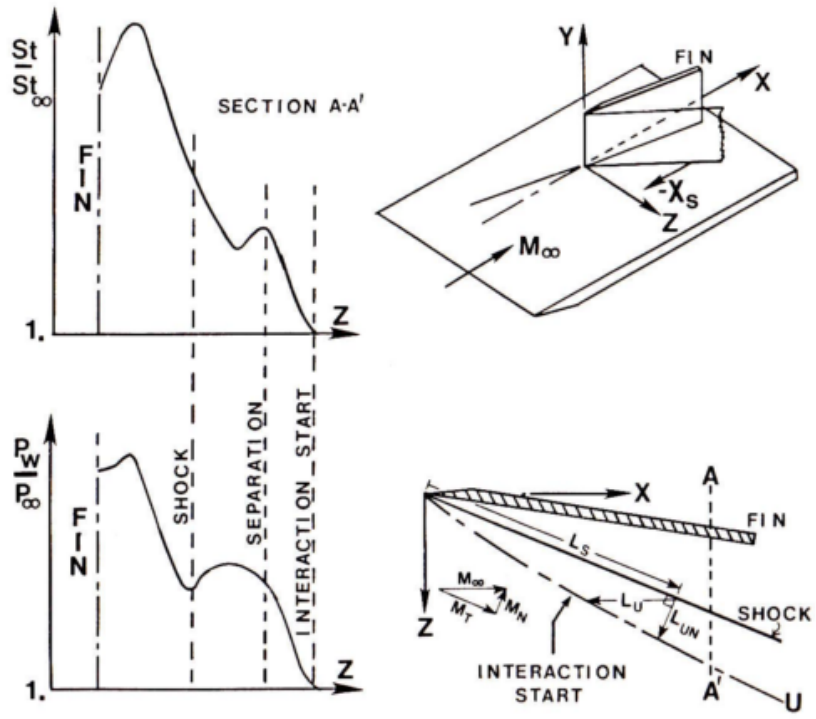

Figure 2.1: Surface Pressure Distribution and Interaction Map of Unswept Fin-Generated SBLI [3]

As discussed above, a small angle of attack and low free stream Mach number do not result in flow separation in the interaction of the shock wave and boundary layer. Korkegi [20] previously defined the relationship for incipient separation as Equation 2.1. The free stream Mach number multiplied with the angle of attack for incipient separation was defined to equal 0.364. This criterion was derived from Stanbrook's [21] definition of incipient separation. Stanbrook defined incipient separation as the condition when the deflected surface oil streaks and the inviscid shock direction are parallel. This definition was refined into a quasi-2D representation by McCabe [22]. Korkegi used McCabe's definition to develop Equation 2.1.

$$M_\infty * \alpha_i = 0.364 \tag{2.1}$$

This equation was later refined by Korkegi [23, 24] to have a value of 0.3 for the constant. The refined version of this equation enjoys considerable acceptance in the scientific

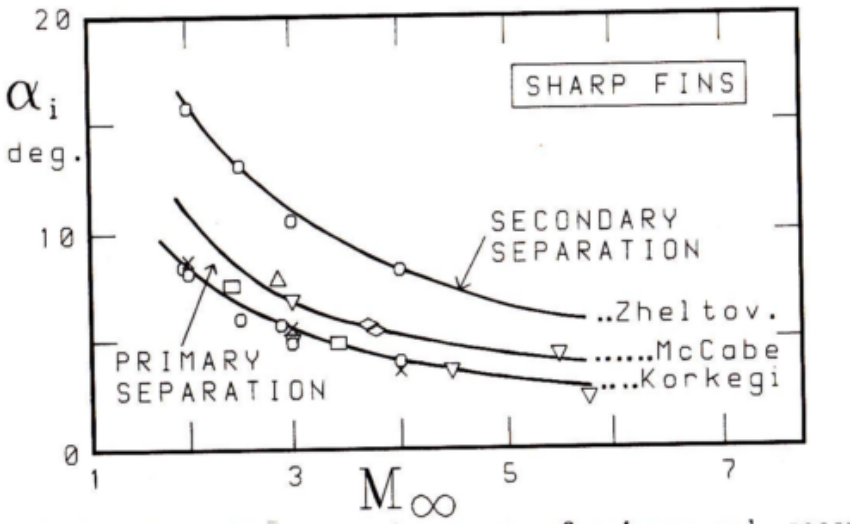

Figure 2.2: Primary and Secondary Separation Conditions [3]

community. One can see that the only flow features used to define separation are the free stream Mach number and the angle of attack. In the present work and prior literature, the normal Mach number has been used to define the interaction "strength". One can see the transition from Korkegi's criterion to the use of normal Mach number does not require major logical leaps.

The secondary separation is a region with a secondary surface vortex inside the primary separation vortex. This condition only arises for very strong interactions. This secondary separation forms in a very complex manner. It was found previously [25] that this separation could appear, disappear, and reappear for increasing α. Figure 2.2 shows the conditions for separation developed from experiments. The primary and secondary separation lines show good agreement with the analytical criterion.

Figure 2.3 shows a graphical representation of the interaction model. This representation includes the secondary separation that exists only at high interaction strengths. The separation shock forms forward of the main shock, and the boundary layer begins to rise after the separation shock. Both the primary vortex (further downstream) and the secondary

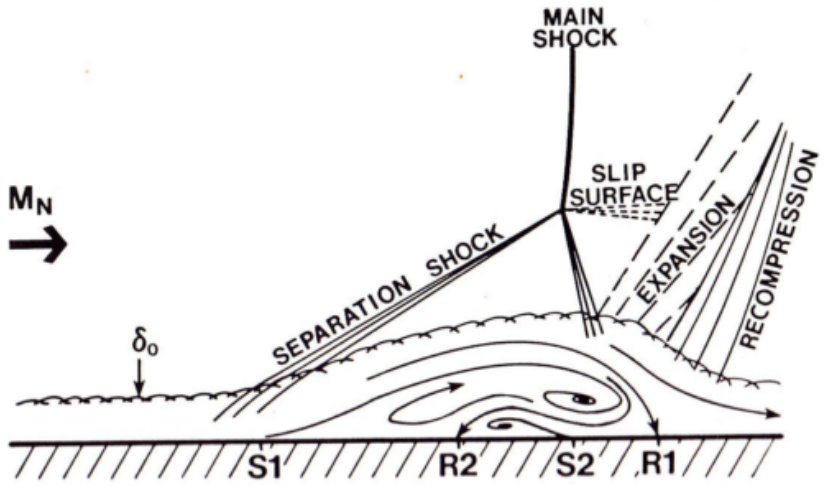

Figure 2.3: Unswept Fin SBLI Structure [3]

vortex (at the wall) can be clearly seen in this figure. Other artifacts present in the interaction are the slip line, expansion and recompression which are all seen in the right of the figure.

Sharp swept fins exhibit a large degree of similarity with unswept fins. While this class of generators has not received extensive investigation, Settles and Lu [26] compared the swept and unswept interactions at Mach 3 and showed that the same structure exists. They plotted Figure 2.4 which shows some of the major features of swept and unswept fin generated SBLI. The vertical axis is the difference between a major feature (upstream influence, reattachment, etc.) and the inviscid shock angle. In this figure, "u" refers to the upstream influence (separation shock), "S1" refers to the primary separation line, "S2" refers to the secondary separation line, and "A" refers to the reattachment. The horizontal axis defines the interaction strength.

2.2.2 Compression Corners

A swept compression corner SBLI generally results in cylindrical or conical symmetry. The convention in these cases is to describe the downstream sweep angle of the corner as λ and the angle between the test section floor and the corner's surface as α. The cylindrically

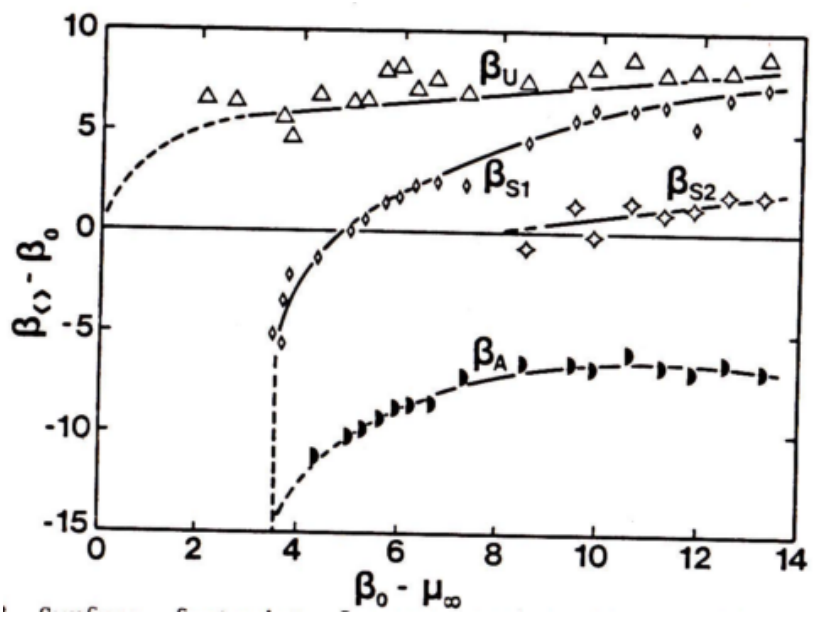

Figure 2.4: Propagation Angles of SBLI Major Features [3]

symmetric regime occurs for low angles of corner sweep (λ). This principle was seen to hold up to $\lambda = 10°$ in previous studies. [27, 28] The cylindrical symmetry yields to conical symmetry with increasing sweep angle. Figure 2.5 shows the boundary between symmetries for varying α and λ at Mach 3. This figure shows the delineation between the symmetry regimes, but it also shows where the separation occurs. There is a portion of the figure that is blocked out. This portion was not able to be explored due to blockage of the tunnel. Overall, it is reasonable to assume that for an increase in λ the flow is more likely to exhibit conical symmetry. For an increasing sweep angle, the flow within the interaction has a larger component of spanwise velocity. One interesting note is that previous experiments showed the cylindrical symmetry to correspond to attached shocks while the conical symmetry condition corresponds to detached shocks.

Figure 2.6 shows the surface pressure distribution of a swept compression corner. In this figure, the flow direction is left to right. As the flow approaches the compression corner, it experiences some compression upstream of the corner itself at the separation shock. This shock results in a sharp pressure increase. Through the interaction prior to the corner, there is a gradual pressure increase. Immediately at the corner, the flow goes through a

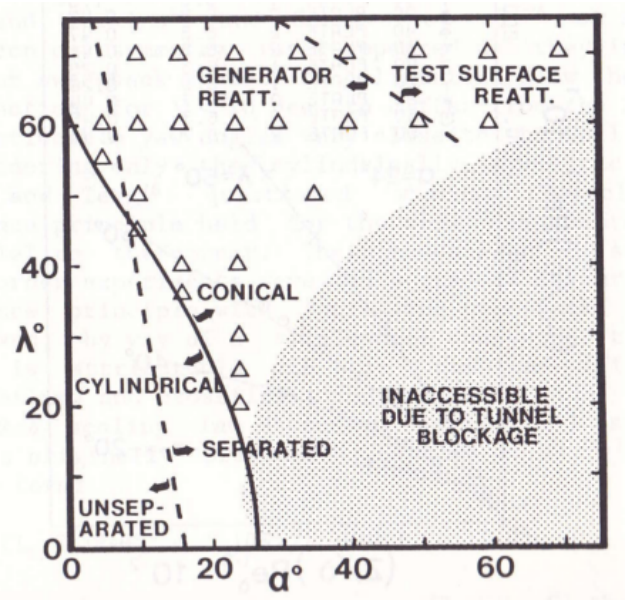

Figure 2.5: Interaction Symmetry Conditions [3]

secondary compression and sees a sharp rise in pressure. This figure shows a comparison of experimental data and computational results. Overall, both results show a similar trend, but it is interesting to note the leveling off and slight decrease in the experimental pressure just upstream of the shock.

2.2.3 Semi-Cones

Semi-cones exhibit many of the same features present in other conically symmetrical interactions. It is relatively intuitive considering the correlation between a semi-cone and a swept compression ramp. One could think of the semi-cone as a two-sided swept compression ramp with a rounded top. This lends itself to a direct correlation between the interaction structures. It was noted [29] that the major factor in this interaction was the combination of the semi-cone angle and the angle of incidence of the cone with respect to the free stream (θ). Interestingly, it was noted that separation occurred at $\theta = 20$, but there were only small effects of the free stream Mach number on the start of separation. One possible reasoning is the highly swept nature of this flow. The cone itself is not very tall away from the floor, so the inviscid shock generated has a large sweep-back angle.

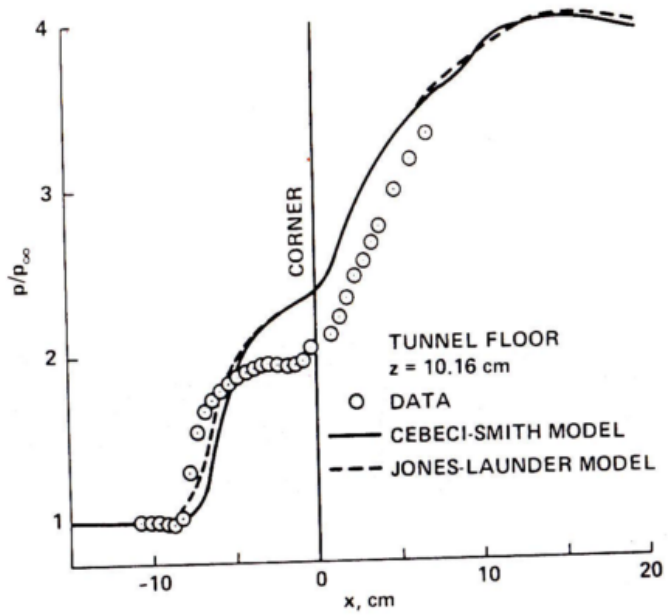

Figure 2.6: Surface Pressure Distribution for a Swept Compression Corner [3]

2.3 Experimental and Computational Results of Conically Symmetric SBLI

This section presents some previous experimental and computational studies of conically symmetric SBLI. The majority of the studies are related to swept and unswept fins, but there is one particular study that shows a different geometry. The primary goal behind the presentation of this particular study is to introduce to the reader the idea that conically symmetric SBLI exhibit many of the same features regardless of shock generator geometry. A secondary goal is to show that the experimental techniques applied in these studies can be used for a variety of different flow geometries.

2.3.1 Hainsworth, et al.

Figure 2.7 shows the experimental setup of an experiment designed to investigate swept SBLI [4]. This experiment used unswept and swept wedges along with planar particle image velocimetry (PIV) to visualize the changes in interaction structure when the sweep angle was increased. The authors used PIV planes at different spanwise locations in order to determine changes in the interaction structure. While this measurement technique is not fully 3D, it

does provide some information about the changes in the interaction with varying spanwise depth. In Figure 2.7a, the left image is an image showing an angled view of a cut through the test section. The right image shows the view from a direction parallel to the spanwise axis of the wind tunnel. The wedge causes an impinging shock on the bottom surface of the test section, and the interaction of this impinging shock with the boundary layer is the portion to be explored. Figure 2.7b shows the location of the PIV planes as viewed from the top of the test section with the impinging shock location marked by the dashed line.

Figure 2.8 shows a shadowgraph of the interaction generated by an unswept wedge. The flow is from left to right. The shadowgraph has the major features marked. The formation of this structure starts with the impingement of the shock on the boundary layer. Similar to an unswept fin generated SBLI, the adverse pressure gradient from this impinging shock causes the boundary layer to turn upward and eventually separate. This separation occurs below the impinging shock with some extent of the bubble forward of the shock. The portion upstream of the impinging shock necessitates the formation of a different shock further upstream to allow the flow to move upward above the separated vortex. In addition, the impinging shock reflects off of the boundary layer. The reflected shock turns the portion of the flow outside of the boundary layer back to its original angle. The flow in the boundary layer that moves around the separation vortex requires another shock to change it to parallel with the flow behind the reflected shock. This forms the final leg of the semi-x shaped shock foot.

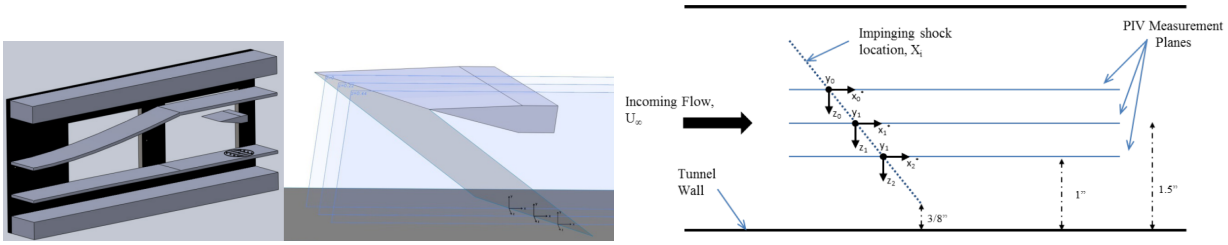

(a) Impinging SBLI Experimental Setup (b) Top view of Impinging SBLI Experimental Setup

Figure 2.7: Plots of Swept Wedge Experimental Setup [4]

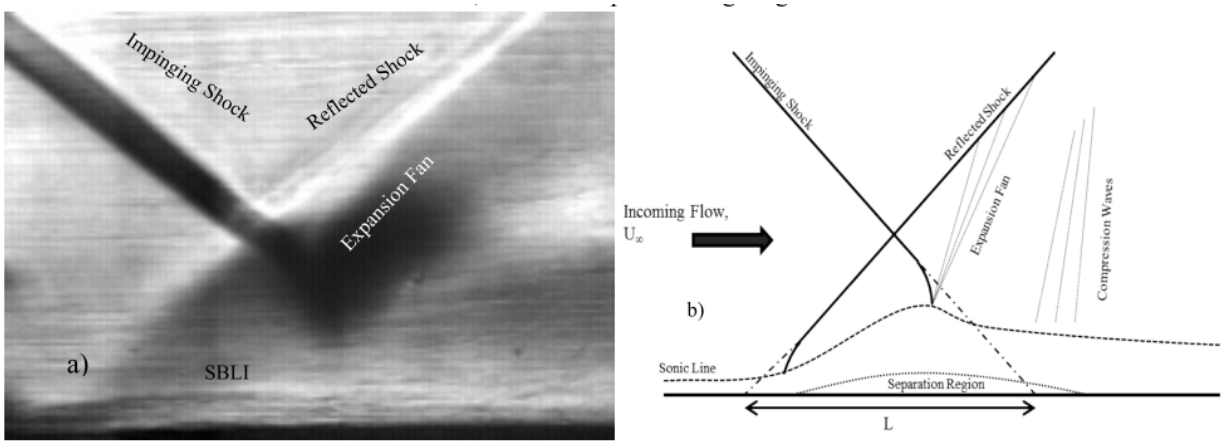

Figure 2.8: Unswept and Swept Wedge SBLI Structure [4]

In Figure 2.8 the impinging shock and reflected shock are marked on both plots. The separation shock is the upstream portion of the shock foot which is seen close to the "a)" in the shadowgraph image. While it is not referred to as a rear shock directly, the rear shock can be thought of as the final portion of the shock foot in the further downstream portion of the boundary layer. This nomenclature allows a more direct correlation to the unswept fin shock foot.

Figure 2.9 shows the results from the PIV experiments. This figure displays the wall-normal velocity normalized by the free stream streamwise velocity. The rows correspond to different PIV plane locations, and the columns correspond to the varying sweep angles. The rows from top to bottom are the planes getting closer to the camera. The columns from left to right are 0°, 22.5°, and 40° sweep angles. One should expect the structure seen in these images because it is known that the flow will turn slightly upward behind the separation shock. This shows itself in the images as the red triangular region. The authors were interested in the changes of these regions with increasing sweep and distance. For the 0° case, there is essentially no change for any change in spanwise distances. There is some changes in the velocity field for the 22.5° case, but the 40° case shows the most change with spanwise distance.

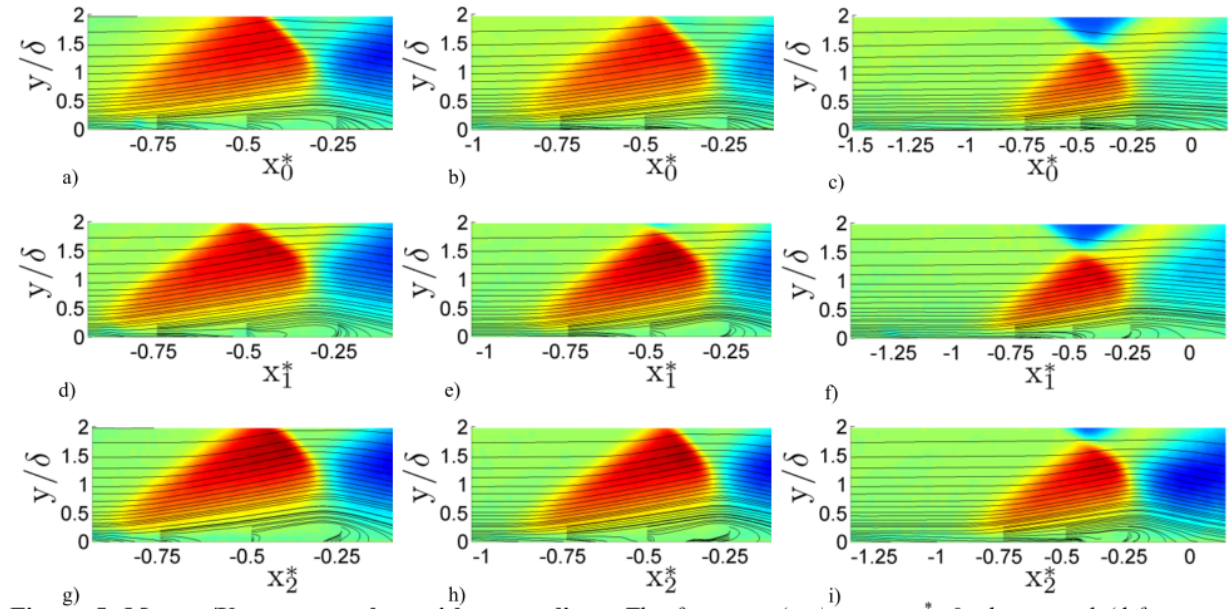

Figure 2.9: Vertical Velocity Contour Plots From Unswept and Swept Wedge SBLI Experiments [4]

Focusing on the 40° case, the 3D effects are most pronounced. The shock foot shows major growth with increasing spanwise distance. This is a feature also exhibited in the unswept fin cases, and it lends itself to the possibility of conical symmetry. In this case the separation bubble is not fully formed at the first plane, but there is fully separated flow shown in the middle plane. The undeveloped separation bubble explains the smaller region of upward velocity in the first plane. As the separation bubble is not fully developed, it has not grown to its full height. This allows the flow above it to remain closer to the test section floor which allows the separation shock to be smaller. Another interesting feature is the apparent decrease in size of the separation bubble with increasing sweep angle. This is likely due to the ability of the flow to move spanwise as well as streamwise for higher sweep.

2.3.2 Fang, et al.

Fang, et al. performed a large eddy simulation on an unswept fin in a Mach 5 flow with a flow deflection angle of 23° [5]. Figure 2.10 shows the setup of the fin and the computational domain. The high Mach number and relatively high angle of attack makes this interaction

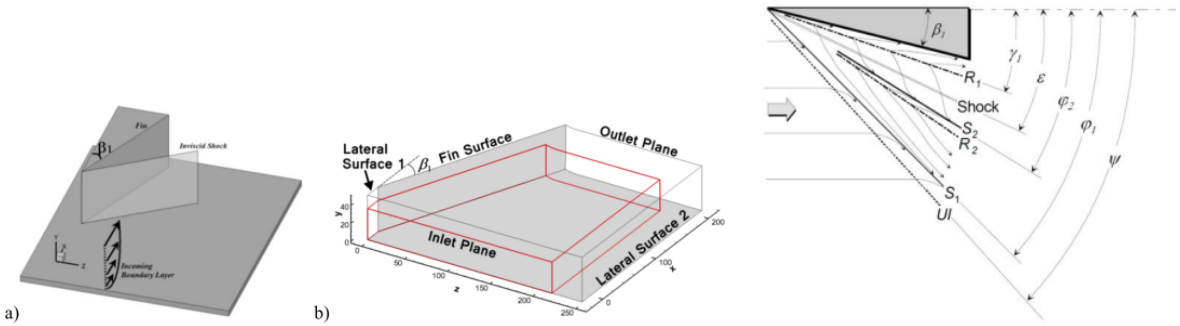

(a) Computational Domain Setup

(b) Top view of Experimental Setup with Feature Lines

Figure 2.10: Plots of Unswept Fin Computational Setup [5]

relatively strong. Figure 2.10a shows two somewhat isometric views of the fin setup and the computational domain. The domain was extended slightly upstream so that the flow would fully develop before the compression from the fin. Figure 2.10b shows a top view of the fin with the lines of symmetry of the major features marked. The features from left to right are as follows: upstream influence (UI), primary separation (S_1), secondary reattachment (R_2), secondary separation (S_2), inviscid shock (Shock), and primary reattachment (R_1). This graphical representation helps to describe the virtual conical origin (VCO) that was discussed earlier. The VCO is the point where the upstream extensions of each of the lines would meet.

Figure 2.11 shows the surface pressure and skin friction coefficient distribution at various streamwise distances. The results are normalized as the spanwise depth divided by the streamwise depth. This allows the scale of the distributions to be the same on the x-axis of the plots. It is important to note that the flow in these images is from left to right. These computational results were also compared with experimental results. One can also look at these figures with respect to the previous figures in this paper and other prior literature to see the same structure in all of these results. The primary separation is seen as the first bump in the pressure distributions. In addition, the secondary separation characteristic of high strength interactions is also seen in these figures. It is interesting to see

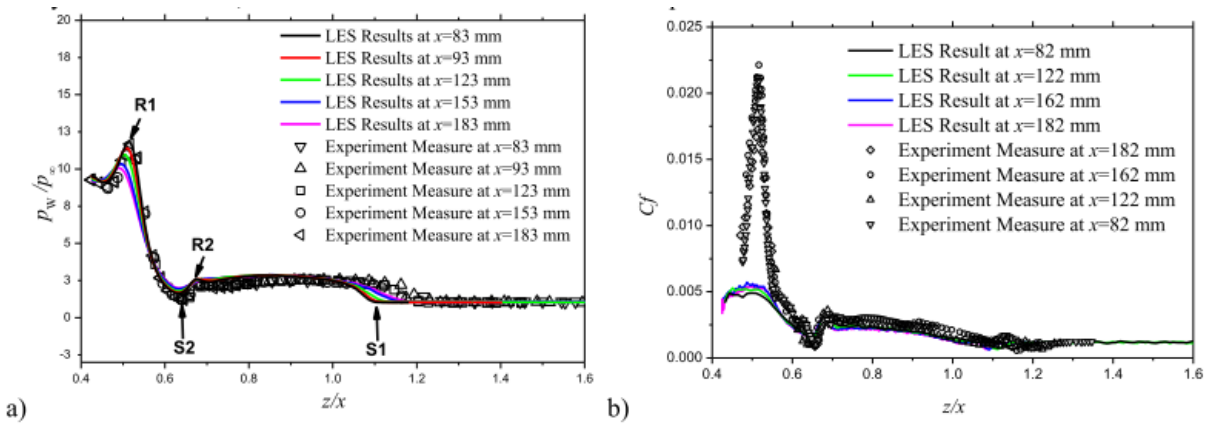

Figure 2.11: Surface Pressure and Skin Friction Distribution From Computational Study of Unswept Fin-Generated SBLI [5]

that the computational results do not conform to the experimental results near the primary reattachment. The authors of this study state that this under-prediction has also been seen in previous LES studies [5].

Figure 2.12 shows an instantaneous numerical schlieren generated from the LES results. This result shows a format that is easier to understand with some of the previous results shown in this paper. This figure breaks down an instantaneous density and pressure gradient field. Figure 2.12a shows the density gradient field, and Figure 2.12b shows the pressure gradient field. This numerical result shows good agreement with the previous results discussed by Alvi and Settles. The present authors have a slightly different terminology. In this study front shock refers to the separation shock and main shock refers to the inviscid shock. It is interesting to see that the rear shock angle is very large. This is likely due to the high interaction strength. One can also notice the normal shock in the impinging jet region due to the strong interaction.

Figure 2.13 shows the mean numerical schlieren results. These results do away with the turbulent fluctuations that provide some clutter to the instantaneous results. This figure shows a very clean view of the interaction structure that is not always seen from experimental results. Due to the high unsteadiness, it is difficult to see the secondary separation bubble, but it is marked by the two center red lines along the x-axis.

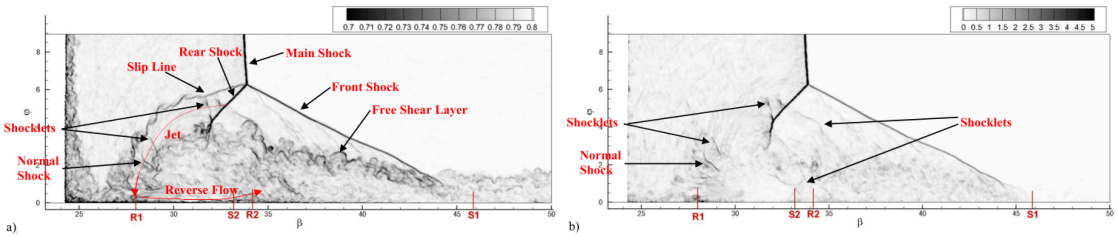

(a) Density Gradient Field (b) Pressure Gradient Field

Figure 2.12: Instantaneous Numerical Schlieren From Computational Study of Unswept Fin-Generated SBLI [5]

Figure 2.14 is used to show a different representation of the computational results. This figure allows a reader to fully understand the direction of all of the points in this interaction. This figure was generated from a semi-circular extraction of the volume, but it can be decently represented by a single plane, as the x-dimension is not extremely large. The authors chose the polar coordinates because it was common in prior literature to use an angular description for the interaction features.

The impinging jet motion contributes largely to the separation and corner vortices. Figure 2.15 shows the stagnation pressure (Figure 2.15a), the static pressure (Figure 2.15b), and the normal Mach number (Figure 2.15c) distributions. In following the flow arrows, particularly in Figure 2.15c, one can see the contribution of the impinging jet to both vortices. It can be seen that the impinging jet turns the flow in two directions at the test section surface, and the flow towards the wall results in a vortex at the corner of the wall. While the changes in each of these properties are known due to compressible flow analysis, it is worthwhile to look at the computational results to see the true breakdown of the pressures in the flow. It is also interesting to see the gradients in the region behind the shock and the separation bubble.

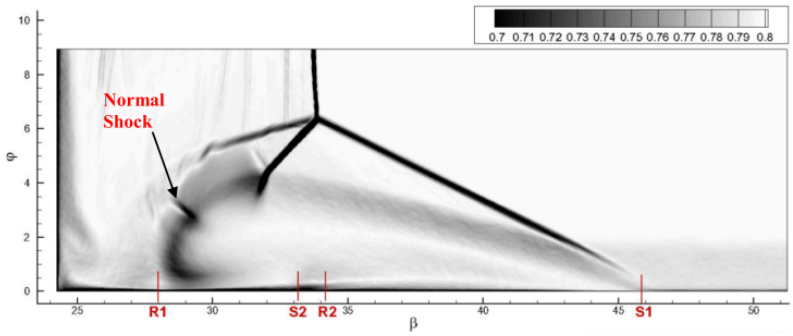

(a) Density Gradient Field

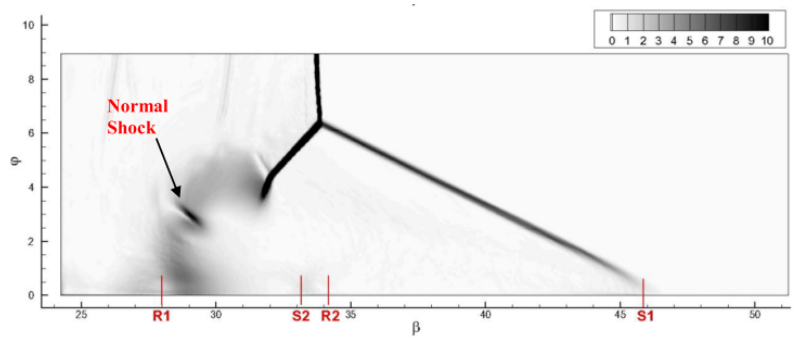

(b) Pressure Gradient Field

Figure 2.13: Mean Numerical Schlieren From Computational Study of Unswept Fin-Generated SBLI [5]

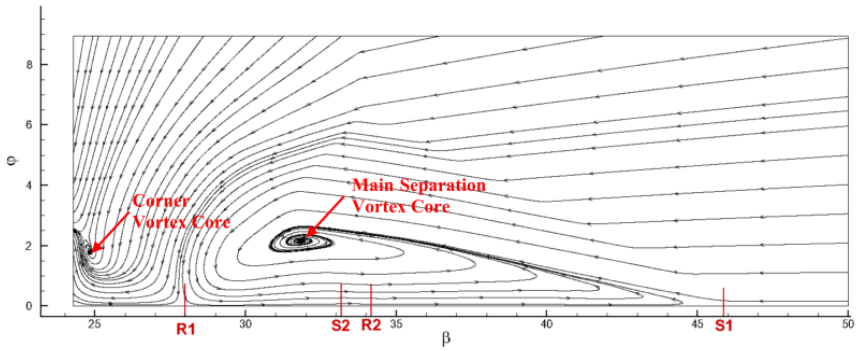

Figure 2.14: Streamlines of the Shock-Normal Velocity in an Unswept Fin-Generated SBLI [5]

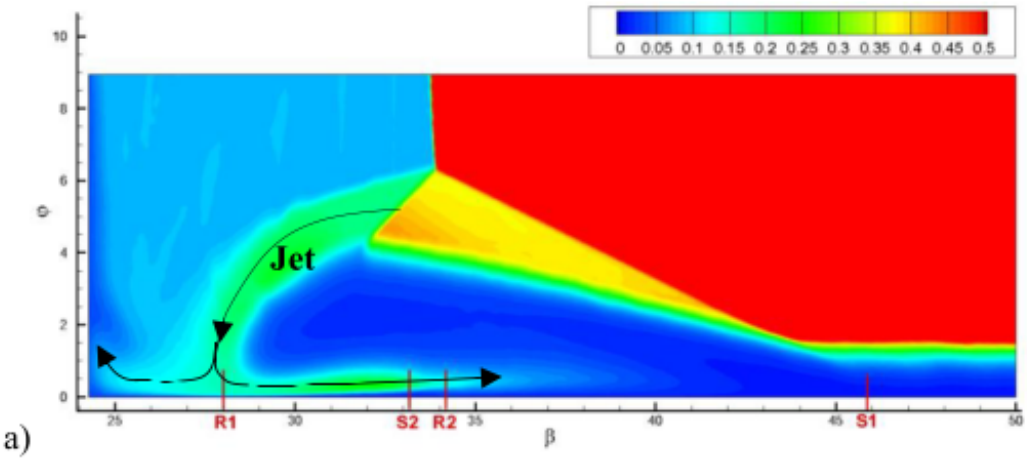

(a) Stagnation Pressure

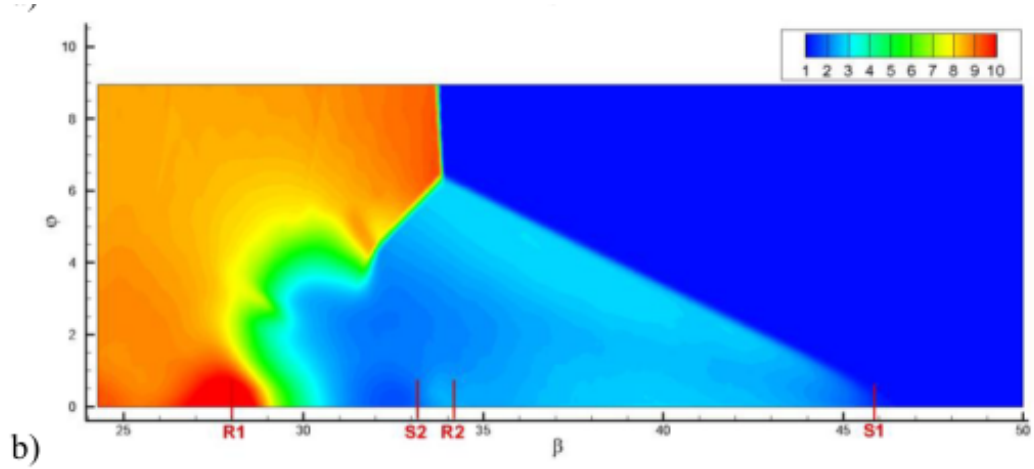

(b) Static Pressure

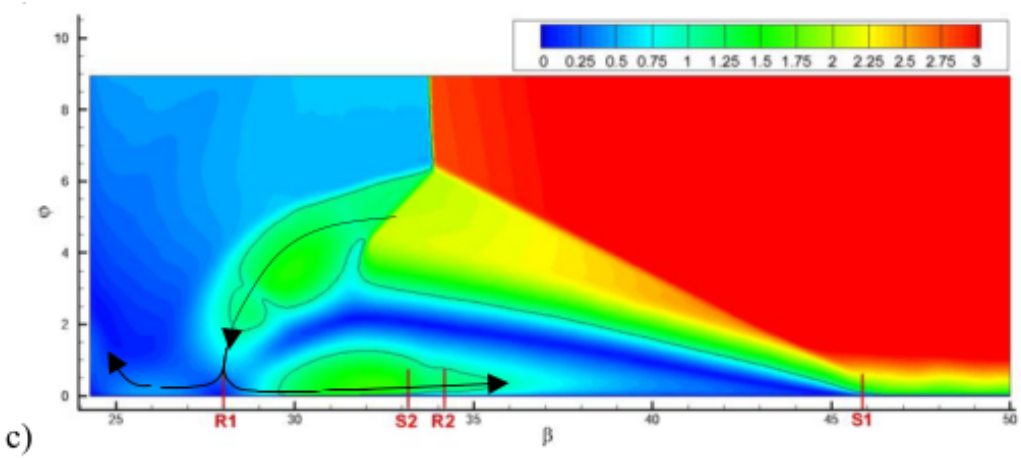

(c) Shock-Normal Mach Number

Figure 2.15: Contours of Pressures and Normal Mach Number in an Unswept Fin-Generated SBLI [5]

2.3.3 Alvi and Settles 1990

While unswept fin generated SBLI have been studied by many authors, one particular study showed a novel exploitation of the conical symmetry of the interaction through the application of a unique subset of shadowgraph imaging called conical shadowgraphy [2]. This imaging technique is based on shadowgraph imaging which uses a collimated light source to visualize density gradients. In the case of an unswept fin SBLI, the fin often prohibits the use of traditional shadowgraphy. In addition, the interaction forms at an angle with respect to the flow direction. This angle can present challenges for line of sight measurements as the density gradient varies only slightly along the entire viewing area. Both of these challenges showed the need for a different technique to visualize density gradients. The authors developed a method where the collimated light source is focused to a single point and therefore propagates in a conical fashion through the volume. Since it is known that the interaction has a conical symmetry, the only major factor is the alignment of the light source's cone with the cone of symmetry of the interaction. This alignment is found when the light source is focused to the interaction's virtual conical origin (VCO). The VCO is not a physical point that is easily measured, and it presents the major challenge to the application of conical shadowgraphy.

Alvi and Settles' experiment provided a quality quasi-2D representation of the interaction structure. Figure 2.16 shows the results from this conical shadowgraphy experiment with increasing normal Mach number from a to d. All of these figures were generated from the same fin at an angle of attack of 20°. The only variation between figures is the free stream Mach number, and therefore the normal Mach number. It is interesting to note in Figure 2.16a that at relatively low normal Mach numbers the interaction has not formed the characteristic λ shock foot. There is a noticeable growth in the boundary layer due to the adverse pressure gradient. As the normal Mach number is increased, the shock foot begins to form. One can also notice that the interaction increases in size (i.e. streamwise dimension, vertical dimension) as the normal Mach number is increased. At this point, it

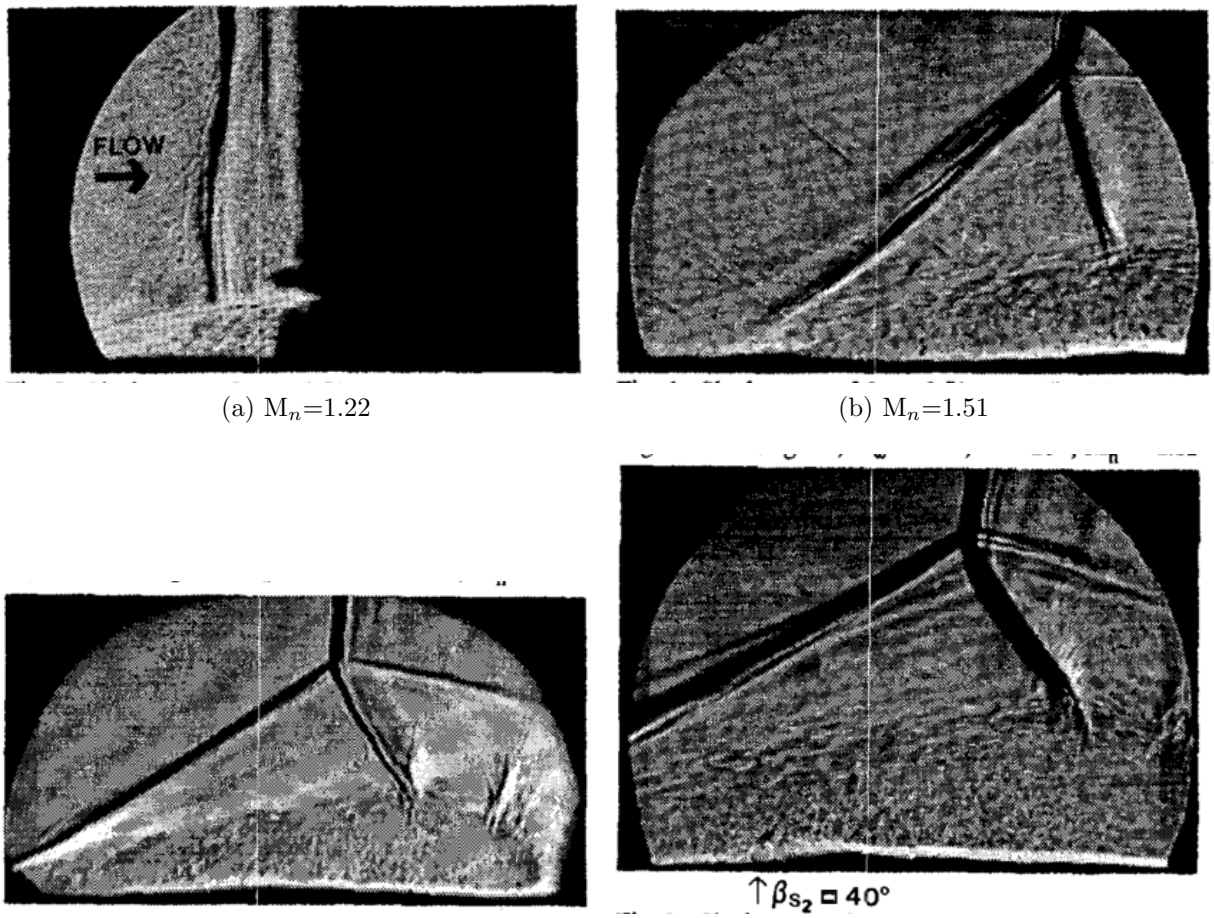

(a) M_n=1.22 (b) M_n=1.51

(c) M_n=1.81 (d) M_n=1.99

Figure 2.16: Conical Shadowgraphy Images of an Unswept Fin-Generated SBLI at Varying Normal Mach Numbers [2]

was necessary to define some value that served as the "strength" of the interaction. Alvi and Settles proposed the use of normal Mach number as this value due to its relation to the freestream Mach number, flow deflection angle, and shock angle. This proposed definition has continued its use even in current research.

Many of the traditional features are shown by the conical shadowgraphy results. The separation shock, rear shock, and slipline are all well resolved. In addition, each of these features presents itself as a single line. This leads to confidence regarding the alignment of the light cone with the VCO. If there was misalignment, the separation and rear shocks especially would likely appear as multiple lines instead of one solid line. Another interesting

feature is the darkening of the region behind the inviscid shock, especially in the lower normal Mach number figures. This is due to the fin's leading edge blocking a portion of the cone of light. As the interaction strength is increased, the inception zone becomes larger and more pronounced resulting in a slight upstream push of the interaction. This upstream push allows the conical shadowgraphy to capture more of the interaction.

Two final features of note from these results are the secondary separation and the normal shock below the slip line. Secondary separation had been discussed as a possibility in previous work, and it was shown in the results here. Particularly in Figure 2.16d one can see the "bump" of secondary separation labeled behind β_{S_2}. This is a section of reversed flow with respect to the previously reversed flow in the separation bubble. This feature has been shown to exist only at high Mach numbers. Another feature that exists only at relatively high Mach numbers is a normal shock below the slip line. This feature was first exhibited in Alvi and Settles' work [2]. This normal shock occurs because the flow behind the rear shock goes through a series of compressions and expansions as it turns toward the test section floor. This necessitates the formation of a normal shock to change the flow before it impinges on the test section floor.

Figure 2.17a is a composite shadowgraph which shows all of the major features seen by Alvi and Settles' [2] work. This shadowgraph is for a free stream Mach number of 3.92 and an angle of attack of 20°. This relatively strong interaction contains many of the features that were discussed above. One can see the slight bump that shows secondary separation. There are also some shock-like structures below the slip line. Figure 2.17b shows the skin friction coefficient and surface pressure distribution. The x-axis in this plot is a value that refers to the angle from the VCO. This leads to a quasi-2D representation as the lines of symmetry remain at the same angle with the exception of the inception zone. One can notice the increase in pressure behind the primary separation line β_{S_1} and the slight decrease in pressure behind the secondary separation line β_{S_2}. In addition, there is a major increase in

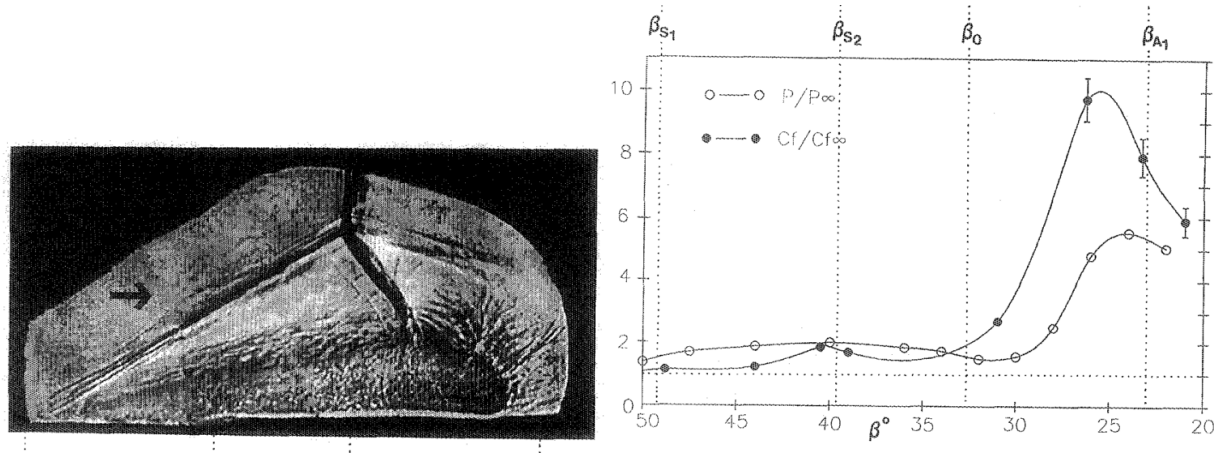

(a) Composite Shadowgraph (b) Surface Pressure Distribution

Figure 2.17: Composite Shadowgraph and Surface Pressure Distribution of an Unswept Fin-Generated SBLI [2]

pressure behind the inviscid shock followed by a decrease near the reattachment line. All of these features are intuitive given a knowledge of compressible flows.

Alvi and Settles [2] were able to extract information regarding the angle of the separation shock and rear shock with respect to the test section floor from their conical shadowgraphy data, and this is shown graphically in Figure 2.18. It is interesting to see that both the separation shock and rear shock angles decrease with increasing normal Mach number. It is also interesting to note the quasi-exponential relationship of both declines. These figures were generated from an increase in the angle of attack of the fin for a specific free stream Mach number. These plots also serve to validate the choice of normal Mach number as representative of the interaction strength. All trials of varying free stream Mach numbers converge well. The decrease of both angles starts from what Alvi and Settles call the "opening up" of the shock foot. For an increasing interaction strength, the shock foot begins to expand greatly in the streamwise dimension. This expansion results in a decrease in the separation and rear shock angles.

Figure 2.19 shows a composite sketch of the features present in an unswept fin generated SBLI. While these features have been previously discussed, it is the intention of the author that this figure serves to clearly define all of the possible features in a single image. This

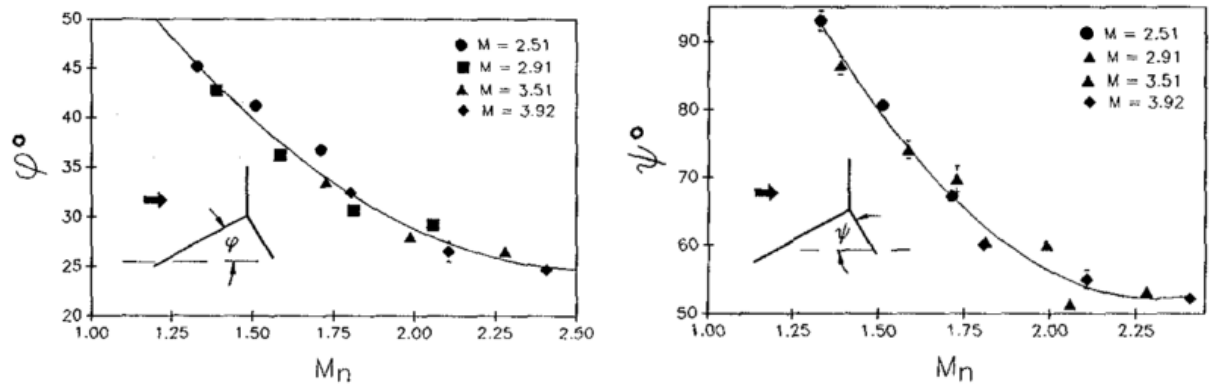

(a) Separation Shock Angle

(b) Rear Shock Angle

Figure 2.18: Plots of Separation and Rear Shock Angles Vs. Normal Mach Number for an Unswept Fin-Generated SBLI [2]

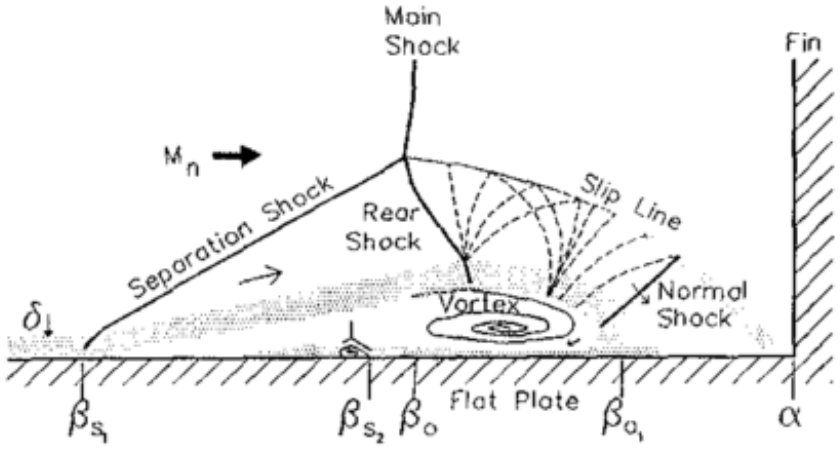

Figure 2.19: Sketch of Unswept Fin-Generated Interaction Features [2]

figure also is more easily understood than conical shadowgraphy or other experimental data. It includes the artifacts that present themselves only at relatively high interaction strengths (the normal shock below the slip line and the secondary separation). It also includes a graphical representation of the expansion that the flow experiences below the slip line. This is a better image showing why the flow accelerates and necessitates a normal shock. It is slightly more difficult to see, but the boundary layer height is marked with δ, and one can see the growth of the boundary layer behind the separation shock.

2.3.4 Alvi and Settles 1992

Another feature worth discussion is the "compacting" of the slip line as termed by Alvi and Settles [6]. The same authors of the previous conical shadowgraphy study also used planar laser scattering (PLS) to obtain the results shown in Figure 2.20. This series of figures shows the interaction structure, pressure, and skin friction coefficients for progressively strengthening interactions. While the separation shock and rear shock angles increase as expected, the slip line becomes progressively shorter. This is an effect not previously discussed for swept SBLI, and unswept fins in particular. This "compacting" of the slip region is largely due to the influence of the fin. As the interaction strength increases, the inviscid shock angle is also increasing. This puts the slip region close to the fin itself. Thus the compacting of the slip region can be thought of as a sort of wall effect (with the fin being the effective wall).

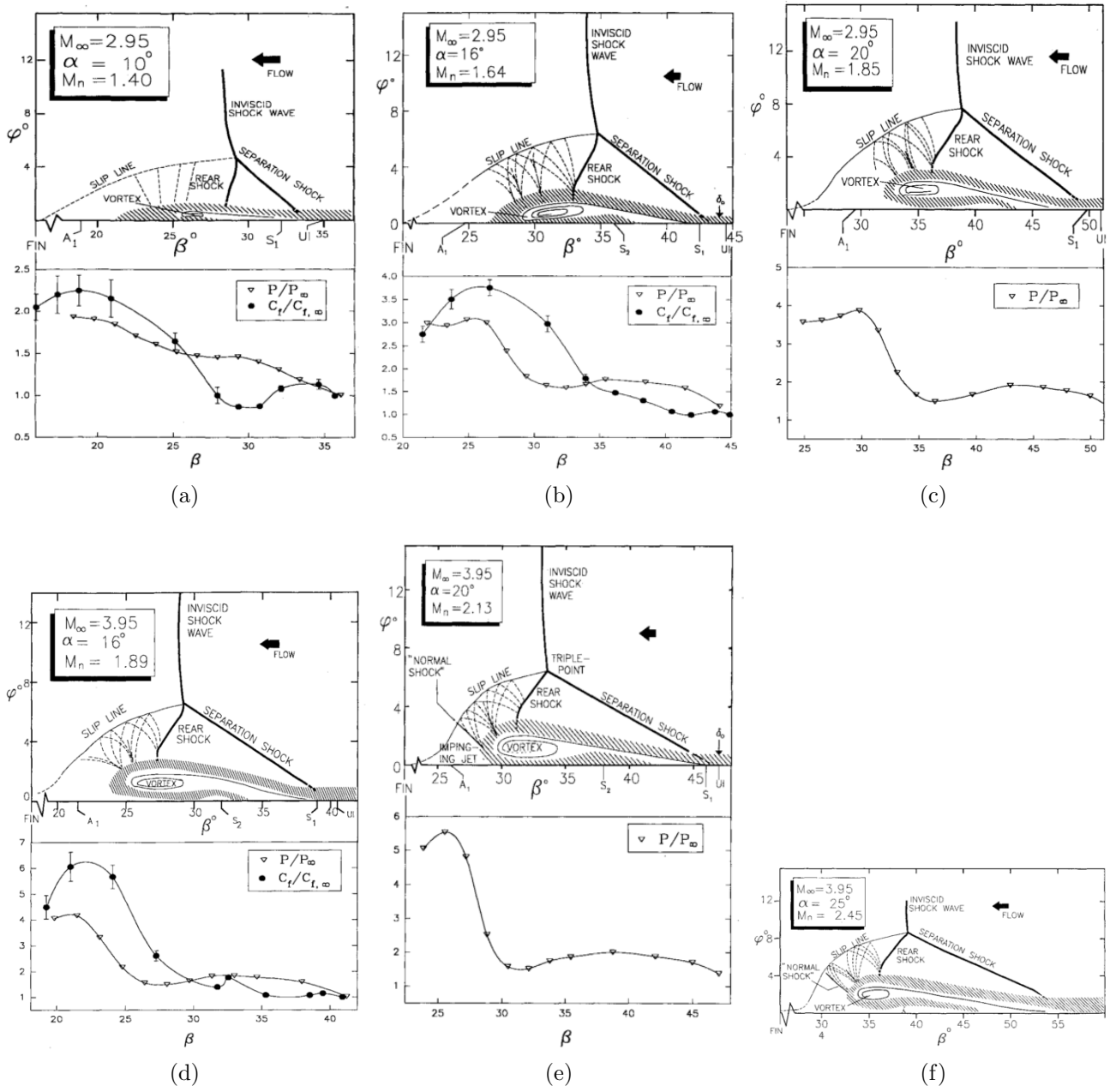

Figure 2.20: Contours of Pressures and Normal Mach Number in an Unswept Fin-Generated SBLI [6]

2.3.5 Arora, et. al

Planar and stereo PIV have been previously performed in the same flow facility at the same conditions as those of the current experiment. [1, 7] This study serves as the major validation for the plenoptic PIV results, and the comparison is discussed in more detail below. Figure 2.21 shows the configuration that the authors used for both the planar and stereo PIV. The unswept fin is marked, and the shock wave angle β is drawn to the dashed line used to mark the location of the inviscid shock wave. The laser plane is shown perpendicular to the inviscid shock. The authors also defined a local coordinate system x', y', and z' to indicate the directions within the plane. The plane was aligned perpendicular to the inviscid shock wave in order to maintain the quasi-2D representation of previous studies as well as the direct comparison to high-speed conical shadowgraphy. The authors of these studies also performed high-speed conical shadowgraphy with the goal of elucidating any particular frequencies of the unsteadiness of the interaction. [7]

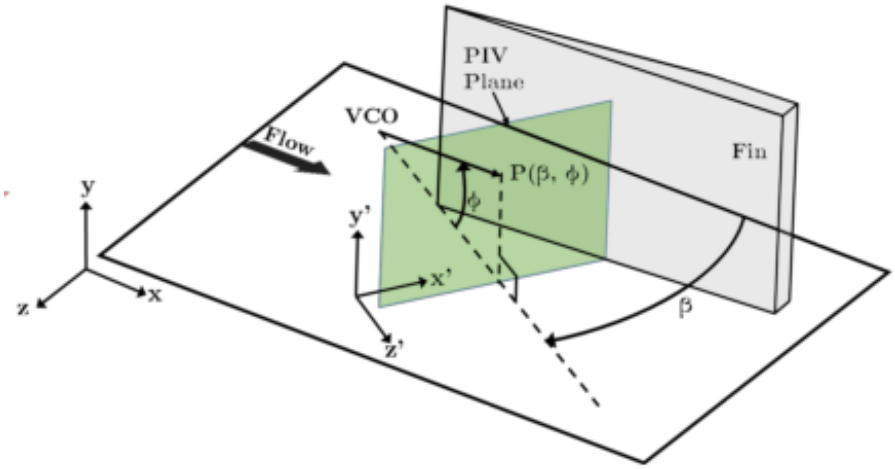

Figure 2.21: Planar and Stereo PIV Experimental Setup [1]

Figure 2.22 shows the surface oil flow visualization produced from this unswept fin in a Mach 2 flow. This figure demonstrates the scope of the conical symmetry, and it shows an excellent representation of the inception region wherein the flow exhibits no symmetry. In addition, this figure demonstrates a method by which the VCO can be found. In this

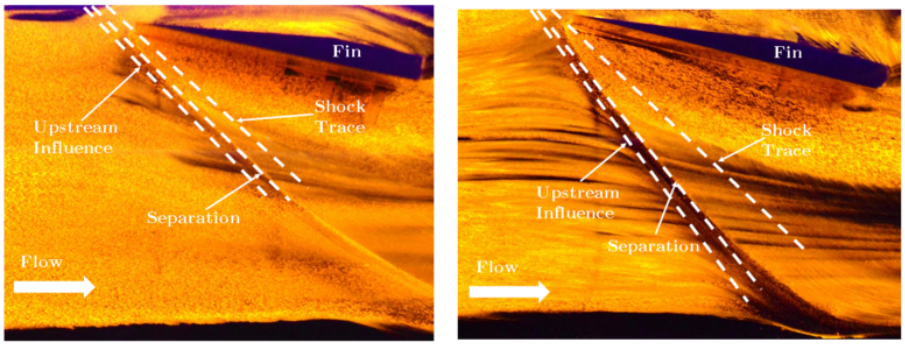

(a) $\alpha = 10°$; $M_n = 1.3$ (b) $\alpha = 15°$; $M_n = 1.4$

Figure 2.22: Surface Oil Flow Visualization of Unswept Fin-Generated SBLI [1]

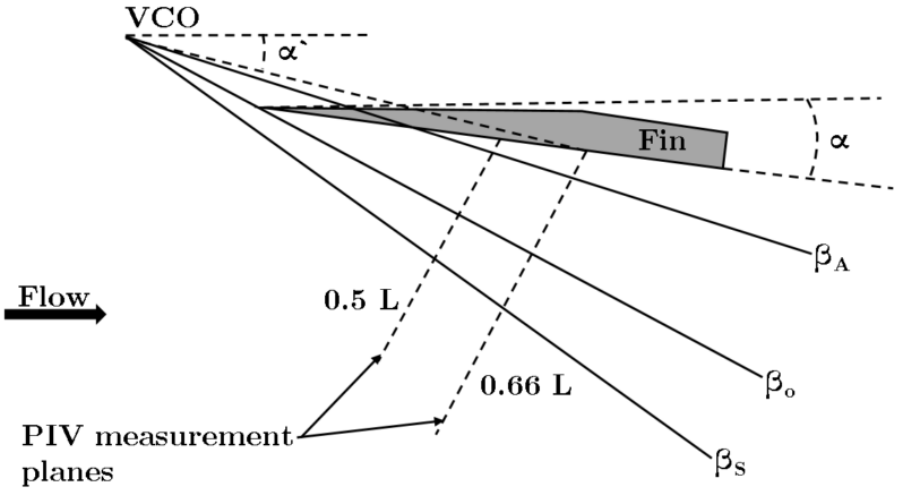

Figure 2.23: Top View of Experimental Arrangement for Planar PIV [1]

study, surface oil flow visualization was used to demonstrate that the PIV planes selected were outside of the inception zone.

Figure 2.23 shows a top view of the experimental arrangement. While this figure is similar to Figure 2.21, it is presented in order to allow the reader to fully comprehend the experimental setup. The two planes chosen for the measurement are marked by dashed lines. These planes were placed at $0.5 * L$ and $0.66 * L$ (length of fin $L = 76.2\,\text{mm}$) in order to exhibit the differences between the interaction size at various depths.

Figure 2.24 shows the in-plane velocity field obtained at both of the measurement planes. The velocity shown is the velocity along the x' direction normalized by the free stream velocity as indicated in Figure 2.21. The expected shock structure can be clearly seen from

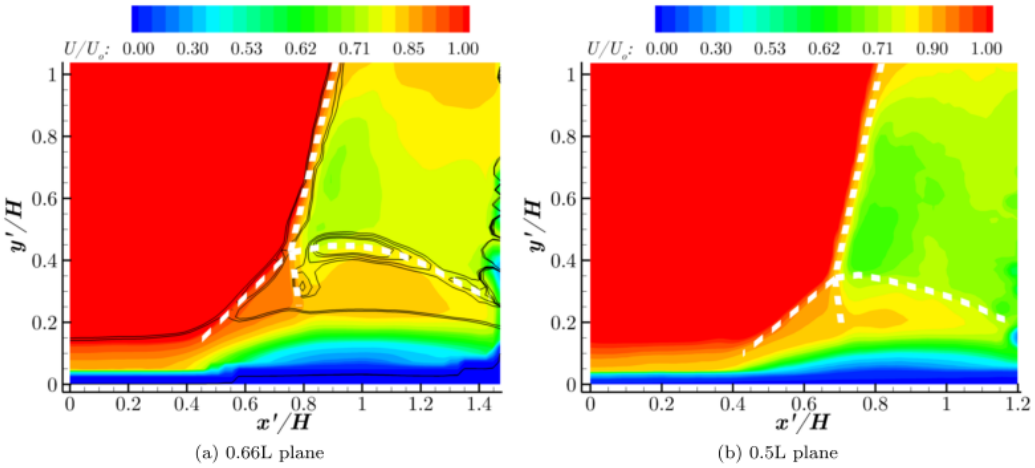

Figure 2.24: Shock-Normal Velocity Contours [1]

the velocity field. The inviscid shock, separation shock, rear shock, and slip line are all marked by dashed white lines. The fully reversed flow inside the separation bubble is seen at the bottom of the image. One major feature of interest is the region of slowed velocity immediately behind the inviscid shock and above the triple point (the point where the inviscid shock, separation shock, and rear shock intersect). This region had not received considerable discussion in previous literature. It is known that there would be some slowing due to the shock wave, but the theoretical solution would result in uniform flow behind the inviscid shock and above the slip line. It is possible, however, that the slowed region is the true flow behind the shock and the relatively fast region near the top of the image is due to the free stream condition above the fin. The fin does not extend across the entire test section, and this finite height likely results in a weakening of the shock wave near the top of the fin. The inviscid shock may curve slightly near the top as it weakens, and this theory is supplemented by the apparent curvature of the contours at the top of the image. It is reasonable to conclude that the faster region near $H = 1$ is due to the influence of the flow above the fin. In addition to this region of interest, the size of the interaction is clearly larger at the $0.66 * L$ plane. This result complies with the knowledge of conical symmetry for the interaction. As the planes get farther away from the fin apex, there should be a clear increase in size (vertical and shock-normal dimensions) of the interaction.

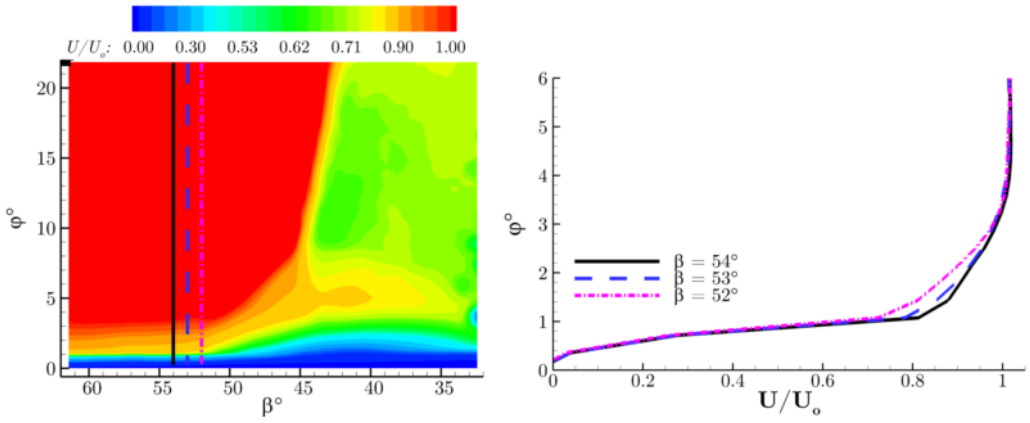

Figure 2.25: Shock-Normal Velocity Contour and profile at various x' distances [1]

Figure 2.25 shows the difference in the shock-normal velocity profile at various distances in the laser plane. This figure is displayed in polar coordinates due to comparisons with previous literature. It is assumed that the laser plane can nearly approximate the surface that is curved in polar coordinates. At small enough distances from the VCO, this approximation is appropriate, but it may not well conform at the distances shown in this figure. Regardless of the accuracy in polar coordinates, a reader can think of the plane in the x' and y' dimensions as shown in Figure 2.24. The results presented here show the boundary layer thickening due to the upstream influence of the separation shock.

Chapter 3

Experimental Setup

3.1 Wind Tunnel Facility

The present experiments were conducted in the Supersonic Wind Tunnel (SST) of the Florida Center for Advanced Aero-Propulsion (FCAAP) on the campus of Florida State University (FSU). The SST is a blowdown-type wind tunnel that is supplied compressed air from a 113 m^3 reservoir. The test section of the SST is 76.2 mm high, 101.6 mm wide, and 393.7 mm long. The tunnel was designed for a Mach number of approximately 2. The stagnation pressure was maintained at 51 psi $\pm$ 1 psi by changing the opening of the control valve throughout the data runs. The stagnation temperature was approximately 296 K. At these conditions the facility is capable of approximately 3 min runtimes, but the data runtimes were limited by the accumulation of seeding on the window of the test section. The test section is capable of optical access from all four sides, but it was configured for optical access from the bottom and one side for this experiment. Most of the optical access is acrylic windows, but for this experiment a glass window was used on the camera side. The fin model was aluminum at 37.5 mm in height and 72 mm in length. The wind tunnel support structure occludes the bottom portion of the test section window from view, therefore, the fin was top-mounted for ease of experimental setup. The facility has a built-in seeder which is a modified Wright nebulizer as detailed by Alkislar [30] which produces seeding particles with a mean diameter of 0.3 µm. The seeding is generated using Rosco fog liquid. The seeding can be introduced simultaneously upstream of the settling chamber and either at the top or bottom of the settling chamber. For this experiment, the seeding was configured for introduction both upstream and at the top of the settling chamber.

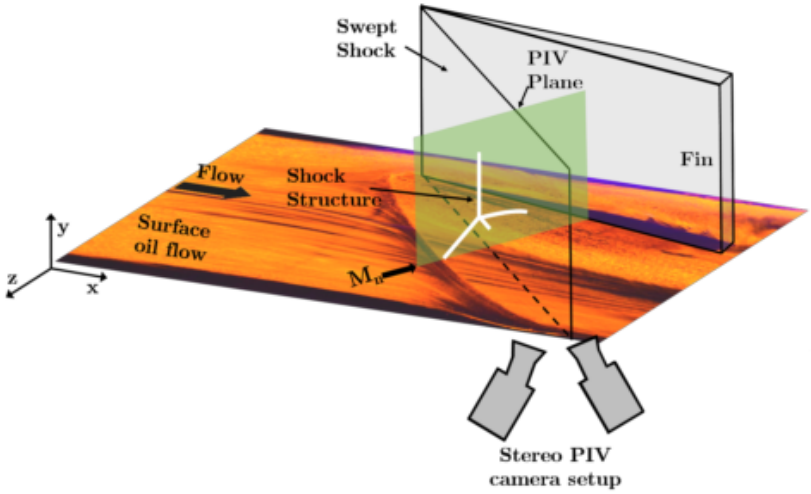

Figure 3.1: Stereo PIV Experimental Arrangement [7]

3.2 Stereo PIV

Stereo PIV was used to investigate both the in-plane and out-of-plane velocities for two different planes aligned perpendicular to the shock axis. Stereo PIV was used both to validate the plenoptic PIV measurement and to determine some 3D effects in the conical frame of reference. Figure 3.1 shows a drawing of the experimental arrangement for a single stereo PIV plane overlaid with a surface oil flow image. Due to the conical symmetry present in fin-generated SBLI, the planes were aligned orthogonal to the shock axis in order to investigate the three-dimensionality of the flow along the shock axis. As a result of optical access limitations, the angle between the cameras was limited to approximately 40°. The test section was coated with Gerber Edge Ready Materials 210 fluorescent film.

These measurements used a Quantel Evergreen Nd-YAG laser with a maximum power output of 200 mJ to illuminate the seed particles. The laser sheet thickness was approximately 2.5 mm. Lavision Imager sCMOS cameras with 2560x2160 pixels were used to image the laser sheet. A 55 mm Nikon lens was used on both of the cameras, and a 532 nm band-pass filter was placed in front of both cameras. The delay time between the laser pulses was 1.8 µs. DaVis 8.2 software was used to obtain the mean velocity field from 1000 image pairs. The final cross-correlation pass was set to 32x32 pixel windows with a 50 % overlap.

3.3 Plenoptic PIV

The plenoptic camera for this experiment was an Imperx B6620. The camera's image sensor was a 29 MP interline CCD (6600x4400 pixels) with pixel pitch approximately 5.5 µm. The microlens array was placed over the image sensor using a custom mount. The microlens focal length was 308 µm. The microlenses were hexagonally packed in a 471x362 array. Each microlens had a pitch of 77 µm which led to approximately a 16x16 pixel grid behind each microlens. The camera's main lens was a Tamron SP AF 60 mm lens with an f-number of approximately 2. As in the stereo PIV measurement, the surface was coated with Gerber Edge Ready Materials 210 fluorescent film, and a 532 nm $\pm$ 10 nm bandpass filter was placed in front of the camera's main lens. The surface coating was enough to reduce some laser flaring, but the camera was still inclined slightly in order to occlude more flaring. The plenoptic camera was aligned with its optical axis orthogonal to the test section's streamwise axis. The plenoptic camera's field of view at the focal plane was approximately 27 mm in the wall normal direction and 40 mm in the streamwise direction.

The laser volume was formed with x, y, and z dimensions parallel to the test section's streamwise, wall-normal, and spanwise axes, respectively. The laser used for plenoptic PIV was a Quantel Evergreen HP with a maximum power output of 400 mJ. The laser volume was formed using two cylindrical lenses with their axes 90° opposed to one another. The laser volume was approximately 40 mm in the streamwise direction and 32 mm in the spanwise direction, and it was introduced from the bottom of the test section. The time between laser pulses was 1.7 µs. The timing was generated using a Stanford Research Systems DG645 digital delay generator and a Quantum Composers 9500 Series pulse generator. The laser's flash lamp limitation was 10 Hz, but the camera limitation was 0.5 Hz (for an image pair, i.e. two images every two seconds). The advanced triggering features of the SRS DG645 were used to prescale the input from the pulse generator by 20. The pulse generator was used to run the flash lamps of both laser 1 and 2, and a third output connected to the input of the

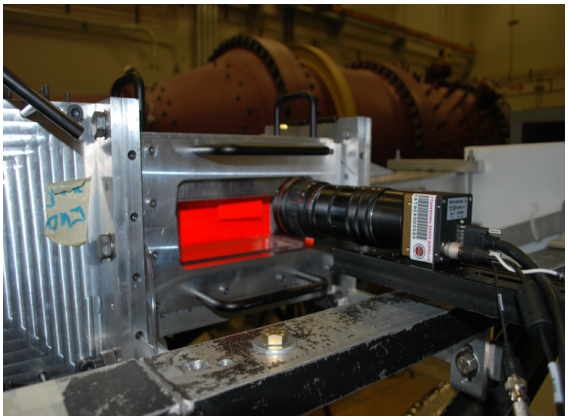

(a) Picture of Experimental Setup

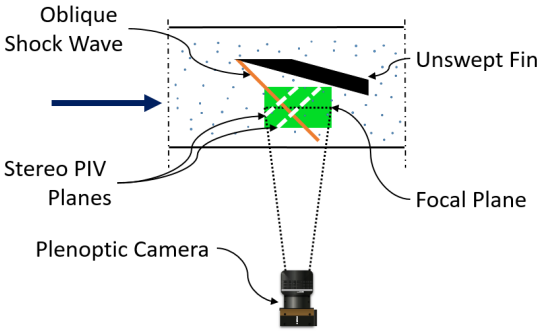

(b) Top View Sketch of Experimental Setup

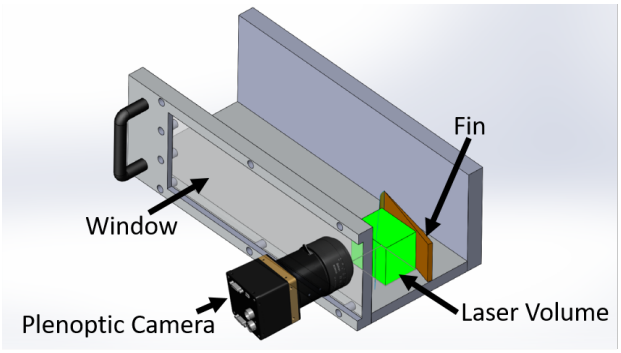

(c) Isometric Drawing of Experimental Setup

Figure 3.2: Experimental Setup Photo and Diagram

delay generator. The input from the pulse generator was scaled, and the delay generator was used to run the Q-switches of both lasers and the camera trigger.

A picture of the experimental setup is shown in Figure 3.2a. The flow direction in this photo is left-to-right. The fin can be seen in the orange region. In addition, a top-view cartoon of the experimental setup is seen in Figure 3.2b. This figure shows the approximate location of the stereo PIV planes on top of the plenoptic laser volume in green. The fin and oblique shock wave are marked, and this figure also shows that the plenoptic camera's focal plane was set to the center of the laser volume. Figure 3.2c shows an isometric drawing of the experimental setup with a better representation of the scale. The fin is colored orange for visibility, and the laser volume is shown in green.

This experiment obtained 555 image pairs during 37 runs. During each run, 20 image pairs were captured, but 5 of each were thrown out due to seeding accumulation on the test section window. The particle volumes were reconstructed using integral refocusing as detailed by Fahringer, et al. [31]. A more common reconstruction method is filtered refocusing, but it was seen in preliminary data processing that the filtered refocusing did not remove much of the noise present due to seeding accumulation. It was seen that the filtered refocusing removed some of the noise caused by laser flaring, but integral refocusing combined with a highpass filter proved to be the best choice for data processing. This effect is demonstrated by Figure 3.3. Figure 3.3a shows a slice of the volume at the focal plane reconstructed using integral refocusing. It is apparent from this image that there is a high noise level in the volume, but particle images can still be clearly seen. It is also apparent from this image that the noise present is a very low frequency noise in comparison to single particle images. Figure 3.3b shows a slice of the volume at the focal plane reconstructed using a filter threshold of 100 and a filter value of 0.8. This filter is not particularly aggressive, but it removes much of the noise around the edges. This filter also appears to remove some particles around the edges of the image, but it does not remove noise or particles in the center of the image. Due to the inability to remove a consistent noise level throughout the volume, consideration was made for alternative options and the integral refocusing with highpass filter was chosen. The volumes were reconstructed to a 545x347x451 grid. In addition, light field calibration as described by Hall, et al. [32] was performed using dot targets placed at five different planes in the volume. The dot target images were taken at the focal plane and at both 7.9 mm and 15.9 mm in front of and behind the focal plane. The dot target had 1.5 mm dots with 3 mm spacing between the inside edges. The dot target was mounted to a rail on the top of the test section in order to traverse in the spanwise direction. The light field calibration serves to minimize any errors due to misalignment of the camera and lens aberrations.

A 3D Gaussian highpass filter was applied to the reconstructed volumes after the integral refocusing to remove the signal associated with the seeding accumulation on the window and

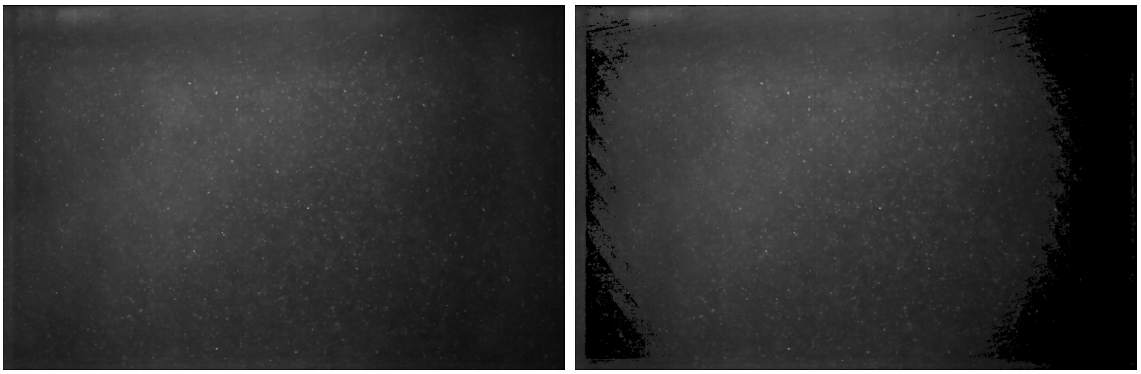

(a) Slice of Volume Reconstructed With Integral Refocusing

(b) Slice of Volume Reconstructed With Filtered Refocusing

Figure 3.3: Slices of Volume with Differing Reconstruction Methods

the laser flaring. Both of these sources resulted in low frequency noise in the volumes, therefore, a highpass filter allowed the particles to remain while the noise was removed. Preliminary data processing utilized a uniform highpass filter with a 9x9x9 kernel. While the uniform filter performed well in removing much of the noise, a Gaussian highpass filter was investigated due to the knowledge that a particle image produces a Gaussian profile. The Gaussian highpass filter had a kernel of 5x5x9. This kernel size was chosen during testing with a simulated single-particle volume. Any kernel size above 9x9x9 was seen to produce errors in the particle volumes. The size was restricted in the x and y axes due to the smaller profile of the particles in those dimensions, and the largest kernel size was used in the z axis due to the particle elongation.

The final step in the data processing was a 3D cross-correlation. An in-house 3D cross correlation algorithm was used to determine the mean velocity field. A five-pass scheme was used, and the final window sizes were 16 voxel cubic windows with 75 % overlap. Each cross-correlation pass had vector validation allowing vectors within 2.5 standard deviations of their local means to pass, and the instantaneous vectors for each position in the volume were filtered allowing vectors within 2 standard deviations of the mean to pass. In addition,

the RMS velocity fluctuations were calculated, and a filter was applied removing fluctuations outside of 2 standard deviations of the mean fluctuations.

Using similar reconstruction algorithms and synthetic image data, the uncertainty in the determination of particle displacement has been previously shown to be approximately 0.25 Voxels in the x direction, 0.48 Voxels in the y direction, and 0.93 Voxels in z direction [31]. Given the grid resolution and the time between laser pulses this uncertainty translates to approximately 10.9 m/s in the x direction, 21.4 m/s in the y direction, and 38.8 m/s in the z direction for individual vectors in an instantaneous volume. Utilizing the presumably steady free stream flow upstream of the SBLI as a surrogate for evaluation of the measurement uncertainty, the RMS of the streamwise, wall-normal, and spanwise components of velocity were observed to be 43.7 m/s, 7.6 m/s, and 41.7 m/s, which is comparable to the analysis given above. It is noted that the uncertainty in the z-direction is the greatest. This is attributed to the limited angular information collected by a single camera system, which leads to an elongated shape of reconstructed particles and broadens the cross-correlation peak along the optical axis of the camera. Additional uncertainty near the boundaries of the measurement volume may also expected as particles translate in and out of the volume between laser pulses.

The primary focus of the current work is on observations made using ensemble averaged velocity data determined from up to 555 image pairs. According to the central limit theorem, the uncertainty in the reported ensemble averaged data will depend on the local velocity fluctuations. Thus, the uncertainty in the ensemble averaged results presented here is estimated to range from 0.2 m/s to 9.9 m/s in the streamwise direction, 0.072 m/s to 3.3 m/s in the wall-normal direction, and 0.1 m/s to 5.6 m/s in the spanwise direction. As will be discussed, the largest uncertainties are found in the recirculation region below the triple point, the region closest to the fin and the corners of the measurement volume.

Chapter 4

Results

Figure 4.1 presents a broad overview of the ensemble averaged 3D velocity field. Figure 4.1a shows a stereo PIV slice overlaid with the plenoptic PIV field of view as a white box. The stereo-PIV plane was nominally perpendicular to the inviscid shock wave and located 38.1 mm from the fin's leading edge. The field of view of the plenoptic imaging volume is conservatively offset from the wall in order to avoid problems associated with surface reflections, but it still captures the location of the triple point and the upper portion of the recirculation region. Figures 4.1b - 4.1f present a 3D representation of the ensemble-averaged 3D velocity field. Figures 4.1b and 4.1c utilize isosurfaces corresponding to velocity magnitude of 462 m/s, 425 m/s and 402 m/s to highlight some of the more significant features of the interaction with Figure 4.1b showing a top view and Figure 4.1c showing an isometric view. The position of the fin relative to the measurement volume is also shown with the origin of the coordinate system located at the point where the leading edge of the fin intersects with the wall. The laser volume's closest corner is 15 mm from the origin in X, 5 mm from the origin in Y, and 16 mm from the origin in Z. Figures 4.1d, 4.1e and 4.1f show 3 different slices of the ensemble average velocity magnitude at locations of Z=10.4 mm, 15.6 mm and 22.4 mm and also indicated in Figure 4.1b.

The red isosurface corresponds to a velocity magnitude slightly below the free stream value and was chosen to highlight the shape of the initial shock encountered by the incident free stream flow. Away from the wall, the inviscid shock's orientation is not quite vertical and is slightly inclined in the downstream direction as also observed in the stereo PIV data. In the top down view, the inviscid shock appears to propagate in a straight line from a point near the leading edge of the fin and forms an approximately 45° angle with the flow

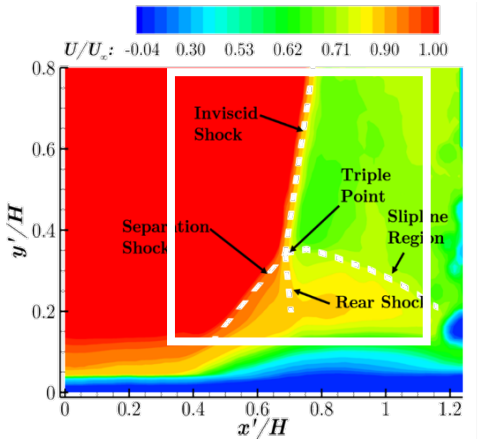

(a) Plenoptic Field of View Overlaid on Stereo PIV Results

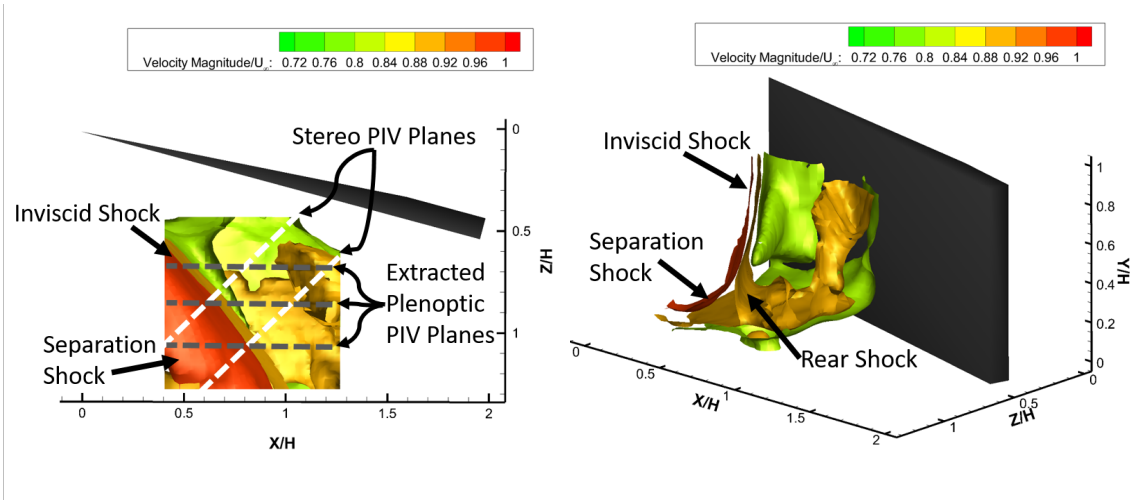

(b) Top View of Velocity Magnitude Isosurfaces (c) Conical View of Velocity Magnitude Isosurfaces

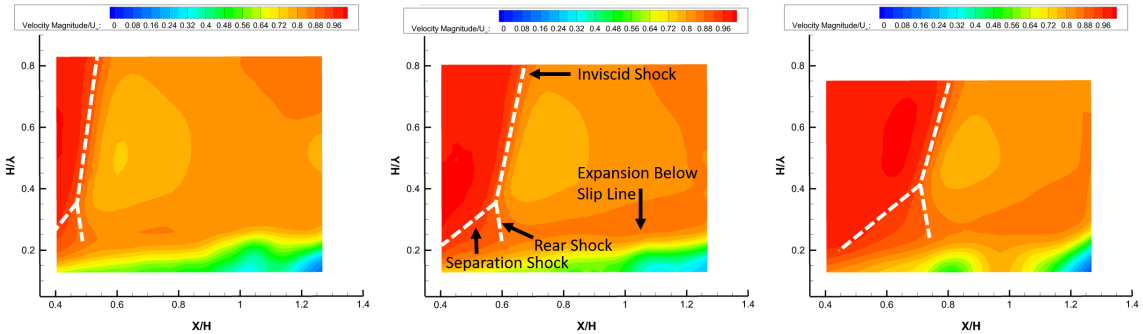

(d) Velocity Magnitude at Z=10.4 mm (e) Velocity Magnitude at Z=15.6 mm (f) Velocity Magnitude at Z=22.4 mm

Figure 4.1: Isosurfaces of Velocity Magnitude

as expected from inviscid shock theory. Closer to the wall, the appearance of the shock foot becomes evident as the shock angle decreases and the shock extends in the upstream direction. This is followed by a gradual decrease in the velocity across the length of the shock foot that terminates with the rear shock whose location is marked using the orange colored isosurface. The size of the shock foot grows with increasing distance from the fin. This is more clearly observed in the 3 slices extracted from the volume where the nominal location of the inviscid shock, separation shock and rear shock are highlighted with a dashed white line. The orange isosurface also marks a region of higher velocity that forms behind the rear shock and has previously been attributed to a series of expansion waves formed in that region. The green isosurface and the remainder of the orange isosurface are discussed subsequently. These overall features of the basic SBLI structure agree well with observations made using shadowgraphy and planar PIV. A noted characteristic of fin-generated SBLI is the presence of a quasi-conical symmetry condition where the growth of the shock foot can be modeled as originating from a virtual origin generally located slight upstream and past the leading edge of the fin. The results presented here support this notion and is particularly evident in Figures 4.1b and 4.1c.

4.1 Comparison with Inviscid Shock Relations

4.1.1 Streamwise Velocity Field

The streamwise velocity field has two major elements according to the inviscid shock relations. The compression due to the fin causes an instantaneous change in velocity, pressure, temperature, etc. Knowing the Mach number and the stagnation temperature of the free stream flow allows a calculation of the free stream velocity. In this flow, the free stream Mach number is 2 and the stagnation temperature is 296 K. The isentropic flow relation and the Mach number equation allow the calculation of velocity. The free stream velocity is approximately 513 m/s. In addition, for a flow deflection of 15° (which is the fin angle of

attack) and a Mach number of 2, the streamwise component of velocity behind the inviscid shock is calculated to be 404 m/s.

Based on the Mach number and the flow deflection angle, the ratio between the streamwise velocity behind the shock and the streamwise velocity ahead of the shock was calculated to be approximately 0.78. In Figure 4.2a, the majority of the streamwise velocity behind the shock is in the 0.8 contour. These numbers show a good agreement between the measured velocity and the theory. It is interesting to note that there are two regions of higher velocity near the rear of the volume as well as one region of slower velocity directly behind the inviscid shock. Figure 4.2a also showcases the major flow features such as the inviscid shock, separation shock, and rear shock. The inviscid shock is the seen in the left of the figure and extends from the top of the figure to approximately the bottom third of the figure. At this point, termed the triple point, the separation shock, rear shock, and the inviscid shock intersect one another. The separation shock is seen in the most upstream velocity changes, and the rear shock is seen nearly below the inviscid shock. The slip line is not extremely well resolved, but this is possibly due to the grid resolution.

4.1.2 Spanwise Velocity Field

The free stream flow is theoretically perfectly streamwise. Behind the inviscid shock the ratio between the spanwise velocity and the free stream velocity was calculated to be approximately 0.21. Figure 4.2c shows a slice of the volume along the z-axis. The spanwise velocity in the free stream region of this figure is not 0, and this effect could be due to a misalignment of the dot cards during calibration. This misalignment could theoretically rotate the entire volume slightly causing an apparent flow toward the fin. Given this possibility, the change in velocity is a more appropriate comparison. It is seen that the free stream spanwise velocity is in the range (-0.05) - (-0.1). After the inviscid shock, the velocity appears to take some time to respond, and it is in the range 0.01 - 0.05. The observed velocity change across the shock wave is not consistent with the expectation from inviscid shock theory. It has been

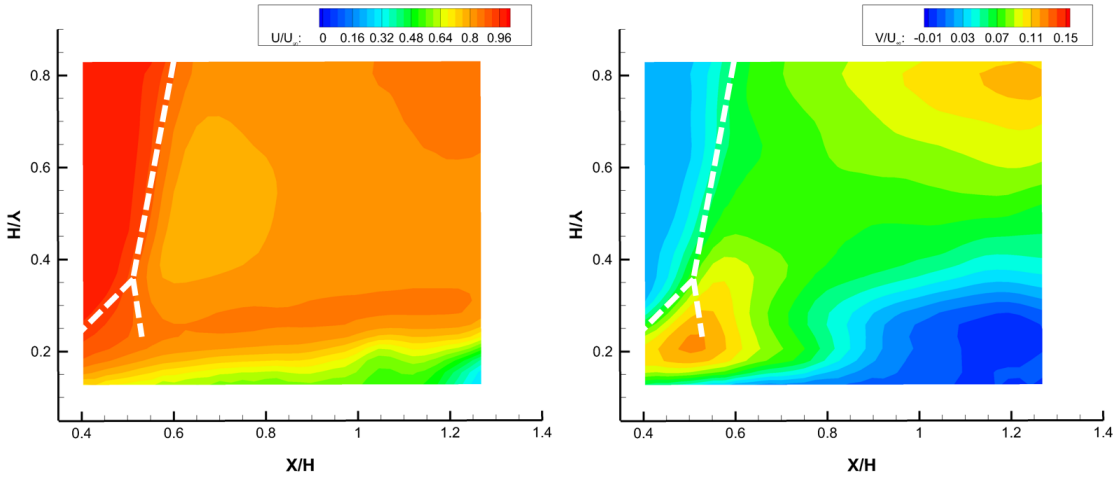

(a) Slice of Streamwise Velocity at Z=12.5 mm (b) Slice of Wall-Normal Velocity at Z=12.5 mm

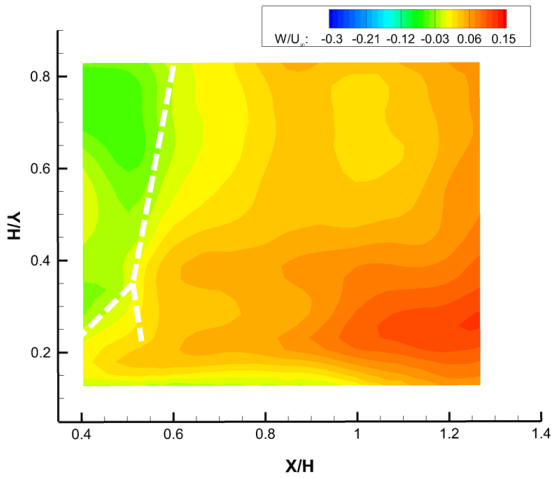

(c) Slice of Spanwise Velocity at Z=12.5 mm

Figure 4.2: Slices of Component Velocities at Z=12.5 mm

previously mentioned that plenoptic PIV suffers from particle elongation in the z-axis. [18] Due to this particle elongation, some error is expected. In addition, there are other factors that could play into the difference in velocities. In particular, a possible 3D relieving effect is discussed below.

Beyond external artifacts, it is apparent that the 2D inviscid shock theory cannot fully describe the flow field. The inviscid shock is clearly not vertical (as seen in prior literature), and the wall-normal velocity shows an upward flow behind the inviscid shock. There is an apparent three-dimensionality in the flow that is not described by simple 2D inviscid shock theory. The 2D inviscid shock theory would describe a planar oblique shock wave, but the angle of the inviscid shock shows that there are other effects present in the volume. In particular, the flow above the top of the fin encounters minimal compression, and this region of lower pressure is likely to interfere with the flow behind the inviscid shock. This interference would likely decrease the pressure ratio near the top of fin causing an apparent incline. In addition, in Figure 4.2b there is an apparent upwards flow in the top right corner of the image. Inviscid shock theory would describe a flow that does not have any velocity component in the wall normal direction. All of these elements show the discrepancy between the experimental results and the 2D inviscid shock theory.

It is interesting to note that the major change in spanwise flow direction appears to align well with the inviscid shock and separation shock. This would indicate that the flow behind the separation shock does turn nearly immediately. While this turn is to be expected, the exact effect and flow direction in this region has not been well-described. While the full effect of this flow on the fully reversed flow at the wall cannot be seen, this is an interesting starting point for future studies.

4.2 Comparison with Stereo PIV Measurements

In addition to validation with inviscid shock relations, it is desirable to validate the plenoptic PIV measurements with a more established experimental technique. The stereo

PIV planes and plenoptic PIV volume were designed to overlap so that this comparison could be made. The stereo and plenoptic PIV experiments were performed at different times, and the stereo PIV was not intended solely as a validation for the plenoptic PIV. There are some possible slight variations in the fin dimensions and tunnel operating conditions. The major difference is the fin thickness as a new set of fluorescent tape was placed on the fin prior to the plenoptic PIV experiment. This new tape was not compressed or deformed due to prior runs in the test section, therefore there is a slight change in thickness. In addition, the plenoptic PIV vector resolution is approximately 1.19 mm in x, y, and z directions while the stereo PIV vector resolution is approximately 0.25 mm in x and y and 2.5 mm in z. This discrepancy showcases the decrease in the ability of plenoptic PIV to capture small scale flow features in the x and y directions. It does show that the plenoptic PIV results are better resolved in the z direction.

The full stereo PIV results have been presented previously. [7] Due to the wave angle being nearly 45°, both the in-plane (shock-normal) free stream and out-of-plane (shock-tangential) velocities according to inviscid shock theory would be the same. Figure 4.3 presents the normalized velocities for the stereo PIV plane at 38.1 mm from the fin apex, and it also presents a slice of the plenoptic PIV volume to match the stereo PIV plane. In both figures, the velocities are normalized by their respective free stream velocity.

It is easy to see that the shock-normal (in-plane) velocities compare well to one another. In the stereo PIV, the inviscid shock is slightly rounded and is slightly angled relative to the vertical direction. A similar observation is made in the plenoptic PIV data, however, the lower resolution masks some of the features. Both data sets show the higher speed expansion region after the rear shock, but the stereo data appears to show a little more detail. In addition, both measurements show variations in property changes across the shock in the vertical direction. In both data sets the free stream flow is seen to be nearly 1, and the velocity behind the inviscid shock is in the 0.6 to 0.7 range for both experiments. The in-plane stereo PIV measurements show a sharp peak around $x/H = 0.46$ and $y/H = 0.2$.

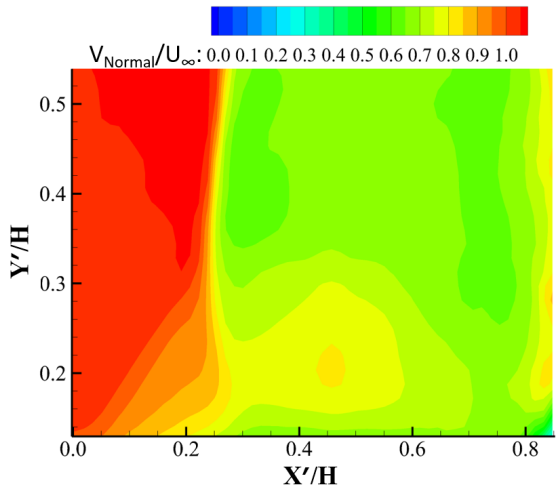

(a) Shock-Normal Velocity from Stereo PIV

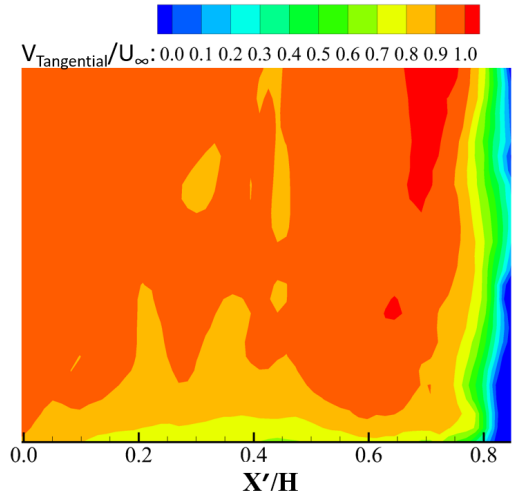

(b) Shock-Tangential Velocity from Stereo PIV

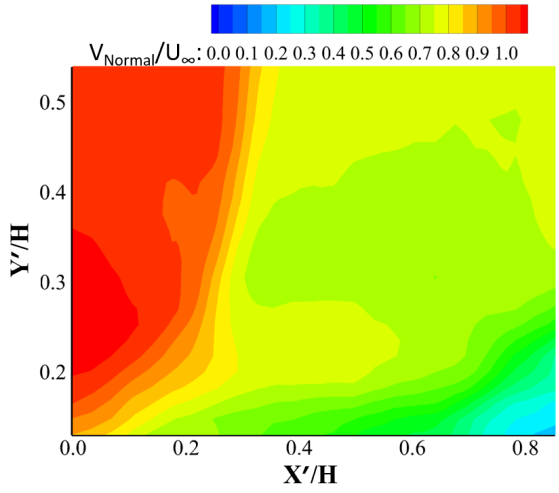

(c) Shock-Normal Velocity from Plenoptic PIV

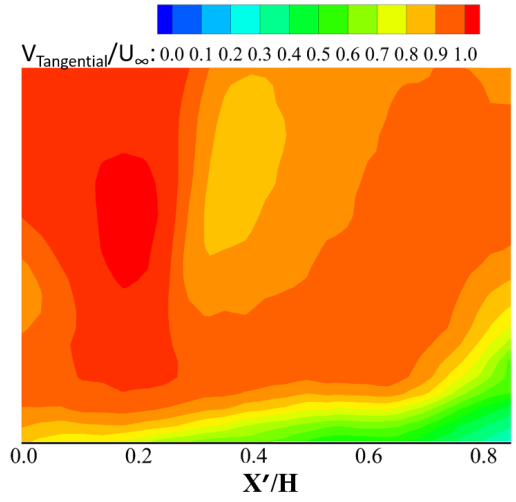

(d) Shock-Tangential Velocity from Plenoptic PIV

Figure 4.3: Slices of In-Plane and Out-of-Plane Velocity from Stereo PIV and Plenoptic PIV

While the overall high speed region surrounding this peak is seen in plenoptic PIV results, the single sharp peak is not seen. This effect is likely caused by the volume resolution of plenoptic PIV. This effect comes from the sacrifice of spatial resolution for the gain of angular resolution in plenoptic cameras. This sacrifice causes a more coarse representation of the velocity field in the plenoptic PIV results.

The shock-tangential (out-of-plane) velocity sees the largest discrepancies. In 2D shock theory, the shock-tangential velocity should remain constant. As discussed above, there are some apparent three-dimensionalities that do not adhere to the 2D theory. The stereo PIV shock-tangential velocity shows some artifacts near the center of the plane. In the plenoptic PIV results, there is a considerable slowing in the shock-tangential velocity behind the inviscid shock. The velocity behind the inviscid shock does recover to nearly 1. With respect to the out-of-plane velocity field, the stereo PIV results show a nearly 20 % decrease in velocity in the center of the plane, but these regions of slower velocity do not appear to correspond to any major flow features. The plenoptic PIV results show a clear decrease in velocity in the region of $x/H =$ 0.3 to 0.55 and $y/H =$ 0.35 to 0.6. It is apparent from this comparison that neither data set fully complies with 2D shock theory. The plenoptic PIV results show a larger decrease in velocity than the stereo PIV results. In addition, the velocity decrease in the plenoptic data set appears to conform to major flow features, but the velocity decreases in the stereo PIV do not appear to conform to major flow features.

4.3 Separation Bubble

The green isosurface in Figure 4.1 shows an outer region of the separation bubble. In this experiment, the fully reversed flow was not captured due to the laser glare from the surface, but the two isosurfaces at the bottom of the volume do show some of the outside of the separation bubble. Another method of visualizing the separation bubble is to show the curvature in the flow near the floor. Figure 4.4 shows two velocity magnitude isosurfaces and a slice of the wall-normal velocity. The most upstream isosurface marks the inviscid shock

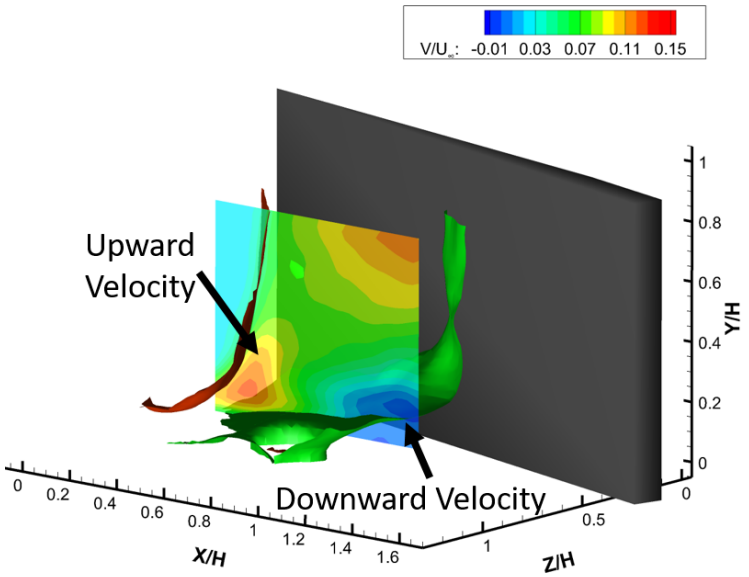

Figure 4.4: Isosurfaces of Velocity Magnitude And Slice of Wall-Normal Velocity at 14.4 mm

and separation shock, and the downstream isosurface marks one level of the slowing toward the fully reversed flow in the separation bubble. One can easily see the upward flow behind the separation shock, and the downward velocity behind the separation bubble is shown in the lower downstream corner of the slice. The entire curvature around the separation bubble is seen from $x/H = 0$ to 0.8 and $y/H = 0.15$ to 0.3. This region frames the separation bubble and the flow that curves around it.

4.4 3D Relieving Effect

Above the fin, the flow sees minimal compression. The flow in this region has nearly the same pressure as the free stream flow. It is important to consider the interaction between this region and the flow behind the inviscid shock. These two regions must be connected in some manner, and the pressure difference would lead to the assumption of an expansion fan. The Mach number behind the shock was found to be approximately 1.44, therefore, it is reasonable to assume the presence of an expansion fan. The pressure difference between the two regions is the likely source of the inclination of the inviscid shock. For a given height

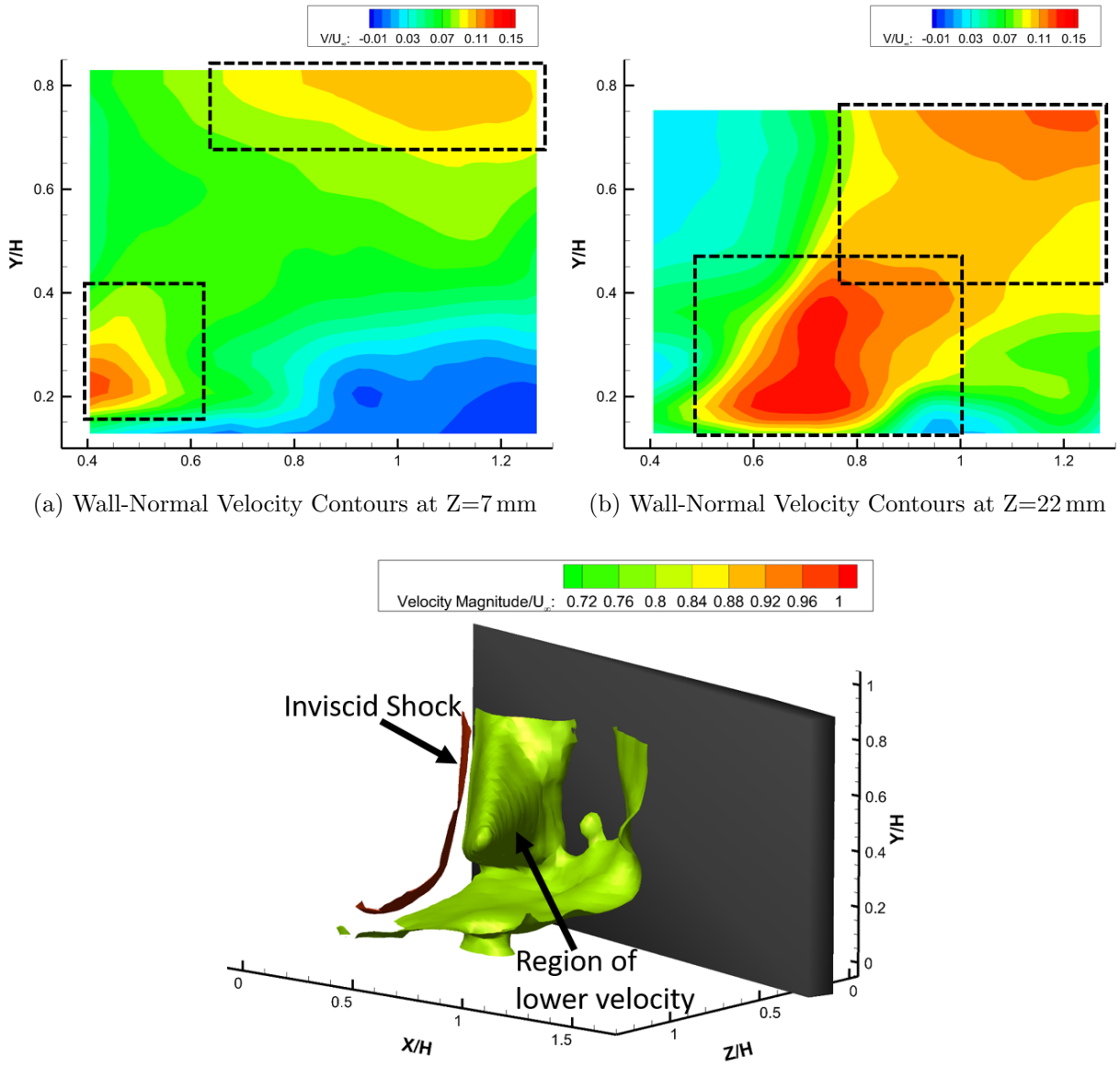

(a) Wall-Normal Velocity Contours at Z=7 mm

(b) Wall-Normal Velocity Contours at Z=22 mm

(c) Isosurfaces of Velocity Magnitude

Figure 4.5: Slices of Wall-Normal Velocity and Isosurfaces of Velocity Magnitude

on the inviscid shock, areas farther away from the fin apex would likely see more influence from the lower pressure region above the fin. This influence would likely cause the shock to incline slightly, and this inclination was mentioned previously.

Figure 4.5 demonstrates some of the 3D relieving effects. In particular, Figure 4.5a shows a z-plane slice of the wall-normal velocity at approximately Z= 7 mm. There is a small region of higher velocity in the region x/H= 0.6 to 0.9 and y/H= 0.6 to 0.85. This region would be intuitive if an expansion fan is present. At areas close to the fin, the flow near the extreme top of the fin would likely increase velocity as it curves over the top of the fin. In contrast, Figure 4.5b shows a slice of the wall-normal velocity at approximately Z= 22 mm. The region of high velocity in the upper corner has moved down into the flow behind the inviscid shock, and a higher velocity contour is seen in the middle. As the expansion fan propagates from the fin tip, for a farther distance from the fin apex its influence would be seen lower in the wall-normal direction. This is particularly shown in Figure 4.5b as the high velocity contours are seen much lower in the volume. There is an interesting effect at the top of this figure, particularly around y/H= 0.8. This apparent slowing is assumed to be an effect of the edge of the PIV volume.

Another way to visualize this relieving effect is that of Figure 4.5c. This figure shows isosurfaces of the velocity magnitude. The inviscid shock is shown for reference, and an interesting conical region is shown by the second isosurface. This is the region of slower velocity seen immediately behind the inviscid shock. It is interesting to note that this region decreases in size with increasing distance from the fin apex, and it does so in a nearly conical fashion. This serves to illustrate the propagation of the expansion fan in 3D. The expansion fan grows larger as it propagates from the fin tip, thus increasing the velocity of the flow behind the inviscid shock and shrinking this region of slower velocity.

4.5 RMS Velocity Fluctuations

In Figure 4.6a a single isosurface of streamwise velocity fluctuations is overlaid on a y-plane slice of the fluctuations. It can be clearly seen that there is a high level of fluctuations present along the inviscid shock wave. This is seen in the isosurfaces propagating at nearly 45° from the fin apex. Interestingly, in Figure 4.6a, the fluctuations around the separation shock are not seen to be consistent in strength. The λ-shock foot is known to be highly unsteady. [33] The velocity fluctuations are reasonably expected to be highest around each of the component shock waves. Due to the strength of the inviscid shock compared to the separation and rear shocks, the inviscid shock is likely to experience much higher fluctuations.

In all parts of the volume, fluctuations around the separation shock were seen, but they appear at different levels. Figures 4.6b and 4.6c demonstrate this feature well. Figure 4.6b shows a z-plane slice of the streamwise velocity fluctuations close to the fin, and Figure 4.6c shows a slice far from the fin. In both figures, the interaction structure can be seen. In Figure 4.6c, the inviscid and separation shocks appear to fluctuate at nearly the same level. In Figure 4.6b, the inviscid shock fluctuations dwarf the separation and rear shock fluctuations. This could be due to some edge effects as the separation shock is very close to the edge of the volume in Figure 4.6c. In addition, the development of the shock foot could play a role as the separation shock may be seen to be stronger when it is farther away from the fin apex. Beyond variations of the separation shock strength, the particle lag time may play a role in decreasing the fluctuations around each shock. The vector resolution as reported above is approximately 1.19 mm, but the inviscid shock in the results spreads over nearly 3.75 mm. This variation would indicate that each vector sees a portion of the velocity decrease but not the entire velocity decrease across the shock.

Figure 4.6 shows some interesting fluctuations near the bottom and edges of the volume. The fluctuations near the bottom of the volume are assumed to be caused by the unsteadiness of the separation bubble. The fluctuations near the fin are assumed to be an element of the volume overlapping the boundary layer on the fin's surface. Further study would be necessary

to determine the source of fluctuations near the fin surface, and current work is focusing on the fluctuations in the separation bubble.

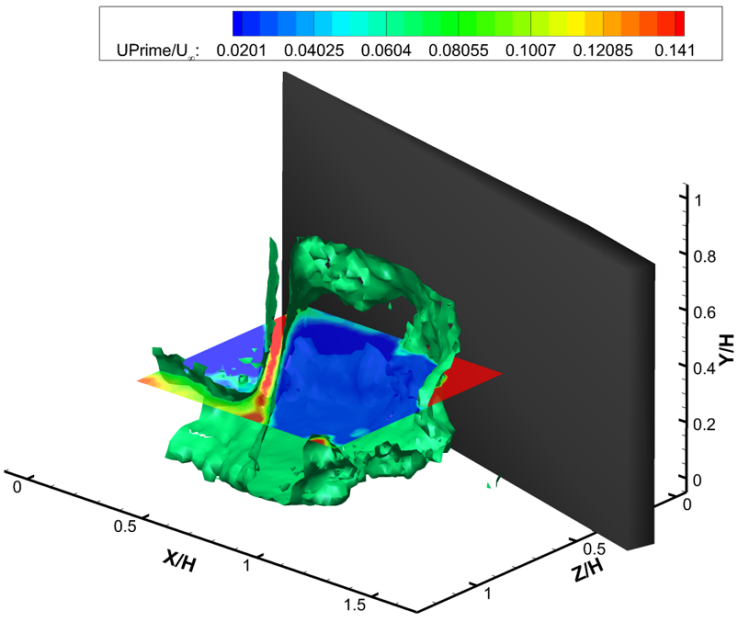

(a) Isosurface With Y-Plane Slice of RMS Streamwise Velocity Fluctuations

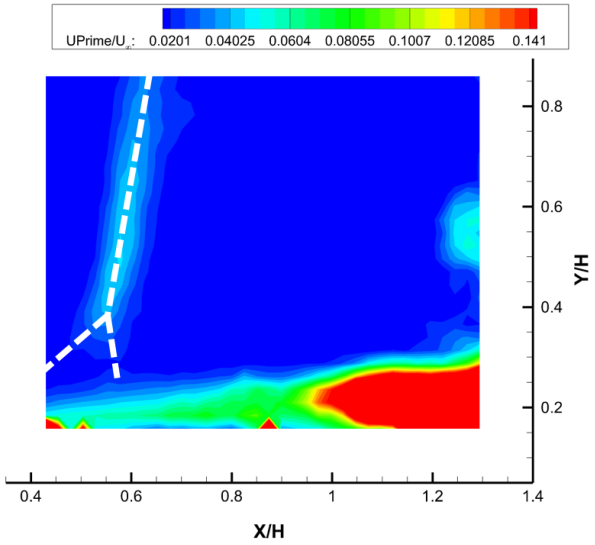

(b) Streamwise Velocity Fluctuation Slices at Z=11.4 mm

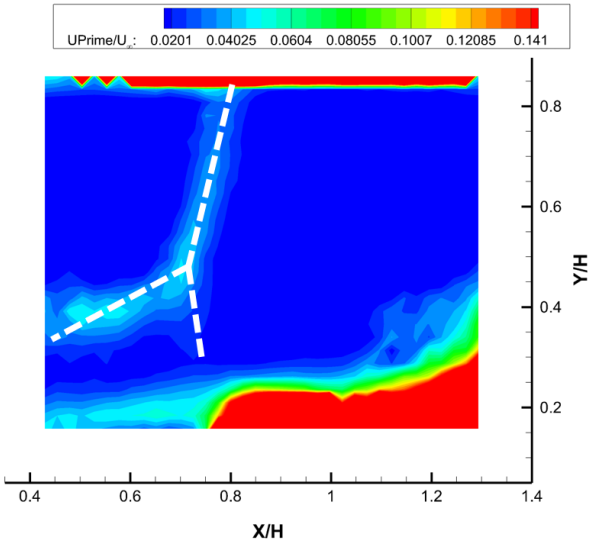

(c) Streamwise Velocity Fluctuation Slices at Z=18.8 mm

Figure 4.6: Isosurface and Slices of RMS Streamwise Velocity Fluctuations

Chapter 5

Conclusions and Future Work

This work marked the first application of plenoptic PIV in a supersonic wind tunnel. This paper used a single camera, 3D measurement technique called plenoptic PIV to investigate the interaction between a boundary layer and a shock wave generated by an unswept fin in a Mach 2 flow. Plenoptic PIV is a highly useful experimental technique that allows a researcher to gain 3D information from a single camera. The results obtained by plenoptic PIV were compared to inviscid shock relations, and the comparison revealed a good agreement between the two in terms of the streamwise velocity component. In the spanwise component, the disagreement between 2D shock theory and plenoptic PIV results showcased the deficiencies of 2D shock theory in describing this complicated, 3D flow field. In addition, the results were compared to stereo PIV measurements in the conical frame of reference, and the results compared well, especially for the shock-normal velocities. Both the plenoptic and stereo PIV results showed 3D features that are beyond the scope of the 2D inviscid shock theory.

Overall, the λ-type shock structure was well-resolved, and plenoptic PIV enabled a fully 3D visualization of the major flow features. While the fully reversed flow was not resolved in this experiment due to laser flaring, the slowed velocity on the outside of the separation bubble was resolved well. The plenoptic PIV results also showed the flow behind the separation shock to turn quickly. Plenoptic PIV also enabled the preliminary investigation of the 3D relieving effect likely caused by an expansion fan. This relieving effect reduced the spanwise velocity of the flow behind the inviscid shock by allowing it to begin to curve over the top of the fin thus increasing the wall-normal velocity. The relieving effect also reduced the pressure ratio near the top of the fin causing an incline of the inviscid shock wave. Finally, the

RMS velocity fluctuations were seen to be greatest around the separation bubble and inviscid shock while the separation shock and rear shock also showed considerable fluctuations.

This study has largely served as a stepping stone for future plenoptic PIV studies of SBLI, particularly in flows that have not been well studied in prior literature. As a matter of fact, at the time of this writing, new studies are ongoing to investigate the fully reversed flow at the wall as well as the effect of actuators in the flow. As another portion of this work, plenoptic PIV is to be used in the polysonic wind tunnel at FCAAP. This newer wind tunnel has a much larger test section and will allow investigation of many more effects of fin-generated SBLI as well as more complicated flow fields. One particular flow field of interest is the shock-shock interaction caused by a double fin. Plenoptic PIV will allow a unique study of the flow features in this geometry. Future improvements in image sensor resolution and microlenses packing would increase the effective volume resolution of plenoptic PIV enabling results that compare better to stereo and tomographic PIV. Two camera plenoptic PIV is being investigated as a means to reduce the measurement uncertainty in the optical axis by reducing the particle elongation. In addition to SBLI, plenoptic PIV is being applied in many other fluid dynamics studies. Prior literature has seen the investigation of porous beds, and current work is even investigating flapping wings. The plenoptic camera is a truly powerful experimental technique that is being developed and applied in many different flow fields.

Bibliography

[1] Nishul Arora, Mohd Y Ali, Yang Zhang, and Farrukh S Alvi. Shock-Boundary Layer Interaction due to a Sharp Unswept Fin in a Mach 2 Flow. In *AIAA SciTech*, number January, pages 1–11, 2015.

[2] F Alvi and G Settles. Structure of Swept Shock Wave/Boundary-Layer Interactions Using conical Shadowgraphy. *AIAA Paper 1990-1644*, 1990.

[3] Gary S. Settles and David S. Dolling. Swept shock wave/boundary-layer interactions. In *Tactical missile aerodynamics: General Topics*, volume 141, pages 505–574. AIAA, New York, 1992.

[4] Jared Hainsworth, Robyn Dawson, and Jesse Little. Experimental Study of Unswept and Swept Oblique Shock- Turbulent Boundary Layer Interactions. In *32nd AIAA Applied Aerodynamics Conference*, number June, pages 1–13, 2014.

[5] Jian Fang, Lipeng Lu, Yufeng Yao, and Alexander A. Zheltovodov. Large - Eddy Simulation of a Three - Dimensional Hypersonic Shock Wave / Turbulent Boundary Layer Interaction of a. *53rd AIAA Aerospace Sciences Meeting*, (January):1–31, 2015.

[6] F. S. Alvi and G. S. Settles. Physical model of the swept shock wave/boundary-layer interaction flowfield. *AIAA Journal*, 30(9):2252–2258, 1992.

[7] Nishul Arora, Mohd Y. Ali, and Farrukh S. Alvi. Flowfield of a 3-D Swept Shock Boundary Layer Interaction in a Mach 2 Flow. *46th AIAA Fluid Dynamics Conference*, pages 1–18, 2016.

[8] Antonio Ferri. Experimental results with airfoils tested in the high-speed tunnel at Guidonia. 1939.

[9] David Dolling. 50 years of shock wave/boundary layer interaction research - What next? *Fluids 2000 Conference and Exhibit*, 2000.

[10] J. Anderson. *Hypersonic and High Temperature Gas Dynamics*. American Institute of Aeronautics and Astronautics, 1989.

[11] J. Anderson and R. Passman. *X-15: The World's Fastest Rocket Plane and the Pilots Who Ushered in the Space Age*. Zenith Press, 2014.

[12] G.R. Inger. Spanwise propagation of upstream influence in conical swept shock boundary-layer interaction. *AIAA Journal*, 25(2):287–293, 1987.

[13] G S Settles and D S Dolling. Swept Shock/Boundary-Layer Interactions Tutorial and Update. In *Tactical Missile Aerodynamics*, pages 297–379. American Institute of Aeronautics and Astronautics, New York, 1986.

[14] Marc Levoy and Pat Hanrahan. Light field rendering. In *Proceedings of the 23rd annual conference on Computer graphics and interactive techniques - SIGGRAPH '96*, pages 31–42, 1996.

[15] Edward H. Adelson and John Y A Wang. Single Lens Stereo with a Plenoptic Camera. In *IEEE Transactions on Pattern Analysis and Machine Intelligence*, volume 14, pages 99–106, 1992.

[16] Kyle C Johnson, Brian S Thurow, Taehoon Kim, Gianluca Blois, and Kenneth T Christensen. Three Dimensional Plenoptic PIV Measurements of a Turbulent Boundary Layer Overlying Rough and Permeable Surfaces. In *18th International Symposium on the Application of Laser and Imaging Techniques to Fluid Mechanics*, 2016.

[17] Timothy W. Fahringer and Brian S. Thurow. Comparing Volumetric Reconstruction Algorithms for Plenoptic-PIV. *53rd AIAA Aerospace Sciences Meeting*, (5-9 January):1–10, 2015.

[18] Tim Fahringer and Brian Thurow. On the development of filtered refocusing : A volumetric reconstruction algorithm for plenoptic-PIV. In *11th Internation Symposium on Particle Image Velocimetry*, Santa Barbara, California, 2015.

[19] Johnathan T. Bolton, Brian S. Thurow, Farrukh S. Alvi, and Nishul Arora. Volumetric Measurement of a Shock Wave-Turbulent Boundary Layer Interaction Using Plenoptic Particle Image Velocimetry. *32nd AIAA Aerodynamic Measurement Technology and Ground Testing Conference*, pages 1–13, 2016.

[20] R. H. Korkegi. On the Structure of Three-Dimensional Shock-Induced Separated Flow Regions. *AIAA Journal*, 14(5):597–600, 1976.

[21] A. Stanbrook. An experimental study of the glancing interaction between a shock wave and a boundary layer. In *British ARC CP-555*, 1960.

[22] A. McCabe. The three-dimensional interaction of a shock wave with a turbulent boundary layer. *Aeronautical Quarterly*, 17:231–252, 1966.

[23] R. H. Korkegi. A Simple Correlation for Incipient-Turbulent Boundary-Layer Separation due to a Skewed Shock Wave. *AIAA Journal*, 11(11):1578–1579, 1973.

[24] R. H. Korkegi. Comparison of Shock-Induced Two-and Three-Dimensional Incipient Turbulent Seperation. *AIAA Journal*, 13(4):534–535, 1975.

[25] A. A. Zheltovodov. Regimes and properties of three-dimensional separation flows initiated by skewed compression shocks. *Journal of Applied Mechanics and Technical Physics*, 23(3):413–418, 1982.

[26] Gary S Settles and Frank K Lu. Conical Similarity of Shock / Boundary-Layer Interactions Generated by Swept and Unswept Fins. *AIAA Journal*, 23(7):1021–1027, 1985.

[27] Gary S. Settles and Jeffrey J. Perkins. Investigation of three-dimensional shock/boundary layer interactions at swept compression corners. *AIAA Paper 79-1498*, 1979.

[28] Gary S. Settles, Jeffrey J. Perkins, and Seymour M. Bogdonoff. Investigation of three-dimensional shock/boundary-layer interactions at swept compression corners. *AIAA Journal*, 18(7):779–785, 1980.

[29] V.S. Avduyevskii and V.K. Gretsov. Investigation of the three-dimensional separation flow around semicones on a flat plate. *Izvestiya Akademii Nauk SSSR, Mekhanika Zhidkosti i Gaza*, 5:112–115, 1970.

[30] Mehmet Bahadir Alkislar. *Flowfield Measurement in a Screeching Rectangular Jet*. Phd dissertation, Florida State University, 2001.

[31] Timothy W Fahringer and Brian S Thurow. Filtered refocusing: a volumetric reconstruction algorithm for plenoptic-PIV. *Measurement Science and Technology*, page 94005, 2016.

[32] Elise M Hall, Timothy W Fahringer, and Brian S Thurow. Volumetric Calibration of a Plenoptic Camera. In *AIAA SciTech*, pages 1–13, 2017.

[33] N. T. Clemens and V. Narayanaswamy. Low-Frequency Unsteadiness of Shock Wave/Turbulent Boundary Layer Interactions. *Annual Review of Fluid Mechanics*, 46:469–492, 2014.